Spatial single-cell profiling of intracellular metabolomes *in situ*

Luca Rappez[1,2], Mira Stadler[3], Sergio Triana[1,2], Prasad Phapale[4], Mathias Heikenwalder[3], Theodore Alexandrov[1,4,5,*]

[1] Structural and Computational Biology Unit, European Molecular Biology Laboratory (EMBL), Heidelberg, 69117 Germany; [2] Collaboration for joint PhD degree between EMBL and Heidelberg University, Faculty of Biosciences, Germany; [3] Institute of Chronic Inflammation and Cancer, Deutsches Krebs-Forschungszentrum (DKFZ), 69120 Heidelberg, Germany; [4] Metabolomics Core Facility, EMBL, Heidelberg, 69117 Germany; [5] Skaggs School of Pharmacy and Pharmaceutical Sciences, University of California San Diego, CA 92093, La Jolla, USA

* Correspondence: theodore.alexandrov@embl.de

-

1

Summary

The recently unveiled extent of cellular heterogeneity demands for single-cell investigations of intracellular metabolomes to reveal their roles in intracellular processes, molecular microenvironment and cell-cell interactions. To address this, we developed SpaceM, a method for *in situ* spatial single-cell metabolomics of cell monolayers which detects >100 metabolites in >10000 individual cells together with fluorescence and morpho-spatial cellular features. We discovered that the intracellular metabolomes of co-cultured human HeLa cells and mouse NIH3T3 fibroblasts predict the cell type with 90.4% accuracy and revealed a short-distance metabolic intermixing between HeLa and NIH3T3. We characterized lipid classes composing lipid droplets in steatotic differentiated human hepatocytes, and discovered a preferential accumulation of long-chain phospholipids, a co-regulation of oleic and linoleic acids, and an association of phosphatidylinositol monophosphate with high cell-cell contact. SpaceM provides single-cell metabolic, phenotypic, and spatial information and enables spatio-molecular investigations of intracellular metabolomes in a variety of cellular models.

Keywords

Spatial single-cell metabolomics, imaging mass spectrometry, microscopy, heterogeneity, metabolic intermixing, macrovesicular steatosis, lipid droplets, cell-cell contact, SpaceM

Introduction

Multicellular organisms contain a multitude of cells of distinct and diverse functions, morphologies, and molecular compositions. Each single cell has a unique intracellular metabolome, a dynamic repertoire of metabolites and lipids involved in virtually all cellular processes. Aside with metabolites and lipids serving as building blocks and energy sources within the cell, recent discoveries unveiled their roles in signaling (Wellen and Thompson, 2012), epigenome regulation (Sharma and Rando, 2017), immunity (Buck et al., 2017), inflammation (Murphy and O'Neill, 2018), host-microbe interactions (Sharon et al., 2014), and cancer (Pavlova and Thompson, 2016). At the same time, the progress of single-cell technologies revealed the extent and biological functions of cellular heterogeneity (Altschuler and Wu, 2010) within tissues, organs (Marioni and Arendt, 2017), tumors (Patel et al., 2014), and even among monoclonal cells in culture (Lee et al., 2014; Pelkmans, 2012; Russell et al., 2018). The discovered critical roles of metabolism and the growing awareness of a hidden world beneath population averages created an urgent need to investigate intracellular metabolism at the single-cell level (Rubakhin et al., 2013; Zenobi, 2013). In the recent years, the sensitivity of mass spectrometry-based metabolite detection has improved substantially opening novel avenues to metabolomics of either single cells or small groups of cells (Do et al., 2017; Guillaume-Gentil et al., 2017; Ibáñez et al., 2013; Merrill et al., 2017) and even at a subcellular level (Passarelli et al., 2017). However, despite these methods successfully demonstrated detection of metabolites in individual cells, analytical and computational challenges precluded studies of spatio-molecular organization and cellular heterogeneity, and prevented discovering the links between intracellular metabolomes, cellular phenotypes and spatial organisation of cells.

55   To bridge this gap, we designed SpaceM, a method for spatial single-cell metabolomics of cell

56   monolayers that integrates MALDI-imaging mass spectrometry with bright-field and

57   fluorescence microscopy. Integration with microscopy enables associating metabolites with

58   fluorescence and morphological cell properties (fluorescent reporter intensity, area, compactness,

59   shape) as well as with spatial features quantifying multi-cellular organization. The integration

60   was enabled by a method for precise detection of parts of cells sampled by MALDI laser with the

61   help of sequential microscopy, novel image analysis, and a novel cell-ablation marks

62   normalisation strategy. Using the False Discovery Rate-controlled metabolite annotation, and

63   novel methods for unbiased selection of intracellular metabolites and for filtering out poor

64   quality cells allowed us to perform high-throughput analyses with >100 metabolites detected in

65   >10000 individual cells, with a high reproducibility between replicates. We validated SpaceM by

66   investigating metabolomes of co-cultured HeLa and mouse fibroblasts cells as well as of

67   differentiated human steatotic hepatocytes stimulated with pro-inflammatory factors that

68   provided rich metabolic, phenotypic, and spatial information.
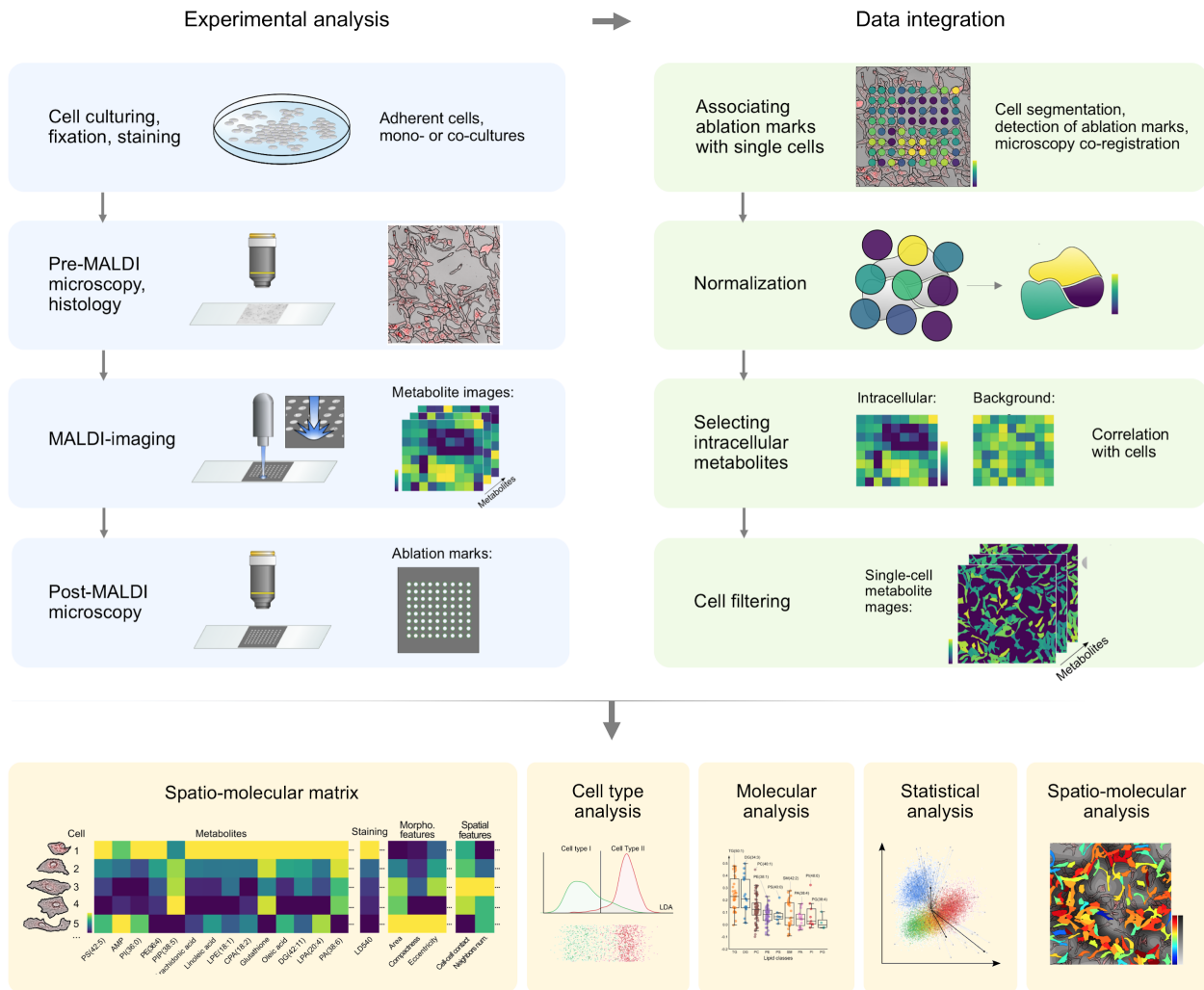
Figure 1. SpaceM method for spatial single-cell metabolomics of cell monolayers by integrative microscopy and MALDI imaging mass spectrometry. *The experimental part of the workflow includes cell culturing, pre-MALDI and post-MALDI microscopy and histology, and MALDI imaging mass spectrometry. The data integration part includes associating of MALDI laser ablation marks with individual cells, strategies for normalization, selecting intracellular metabolites, and cell filtering (see Figure S1 for a detailed workflow). SpaceM outputs a single-cell spatio-molecular matrix providing rich information for a variety of analyses, in particular to characterise cell types, associate single-cell metabolomes with a fluorescent phenotype,*

78   *interrogate changes of single-cell metabolomes upon perturbations, and discover spatio-*
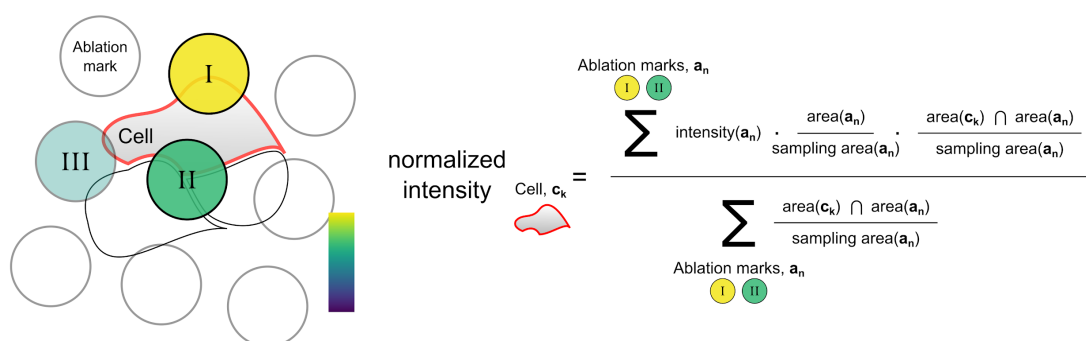
79   *molecular associations.*

80

Results

82   **The SpaceM method**

83   SpaceM relies on using Matrix Assisted Laser Desorption Ionization (MALDI)-imaging mass

84   spectrometry, a spatially-resolved mass spectrometry technology for detection of a wide range of

85   molecules (Baker et al., 2017). MALDI-imaging is increasingly used for spatial metabolomics

86   (Palmer et al., 2016) and was demonstrated to achieve the femtomolar-levels sensitivity

87   (Soltwisch et al., 2015). This, together with soft ionisation preventing excessive in-source

88   molecular fragmentation makes it a perfect choice for single-cell metabolomics as demonstrated

89   by others (Do et al., 2017; Ibáñez et al., 2013). The experimental part of SpaceM combines

90   MALDI-imaging with microscopy as well as with collecting supporting information to integrate

91   these two sources of data (Figure 1; for a detailed workflow see Figure S1). The cells for

92   SpaceM are cultured on a labtek chamber glass slide in a monolayer, with the cell confluence

93   sufficient to allow cells to interact between each other but at the same time preventing the growth

94   of cells on top of each other. After washing, cells are fixed to halt enzymatic activity, stained

95   with a fluorescent dye with the staining protocol compatible with metabolomics, and dried in a

96   desiccator following regular cell preparation protocols. SpaceM requires the Hoechst (or any

97   similar) staining for nuclei detection. For investigation of the steatotic hepatocytes, we also used

98   the lipophilic LD540 staining to detect lipid droplets (Spandl et al., 2009). Then, bright-field and

99   fluorescence microscopy images of cells are collected with the following two aims in mind.

100   First, the cell segmentation of the microscopy images provides cell outlines and enables cell

101   localization. Second, microscopy provides rich phenotypic information about single-cell

102   fluorescence, immunochemistry and spatio-morphological properties of the cells. In the next

103   experimental step, MALDI-imaging is applied to the dried cells to collect mass spectra across

104   cells and extracellular areas. MALDI-imaging procedure starts with application of an ionisation-

105   enhancing matrix. Similar to MALDI-imaging of tissues, we used a robotic sprayer for enhanced

106   extraction, high spatial resolution, and high reproducibility. MALDI-imaging generates big

107   datasets with millions of mass-to-charge channels. For finding metabolic signals in this data, we

108   exploited the False Discovery Rate-controlled metabolite annotation implemented as the

109   METASPACE cloud software (http://metaspace2020.eu) (Palmer et al., 2017). METASPACE is

110   an essential step as it reduces millions of mass-to-charge (m/z)-values to ~100 metabolite

111   annotations, filters out signals representing matrix and contaminants, ensures quality control and

112   represents metabolite images a user-friendly way. In the last experimental step, we performed

113   post-MALDI microscopy to determine which cells were sampled by the MALDI-imaging laser

114   and to associate MALDI-imaging spectra with the cells. Next, we performed data integration

115   with the first step associating ablation marks with individual cells. We detected MALDI laser

116   ablation marks in post-MALDI microscopy images using a customized 2D Fourier

117   Transformation image analysis method that exploits similarities between ablation marks and the

118   regularity in spacings between them. Then, we obtained positions of the MALDI-imaging

119   ablation marks within the cell areas by co-registering pre-MALDI microscopy images

120   (containing cell outlines) with post-MALDI microscopy images (containing ablation marks

121   outlines) (Figure S2). For a majority of cells, a cell was sampled with just one ablation mark. In

122   our benchmarking experiment with HeLa cells and NIH3T3 fibroblast (described later), 72.25%,

123 23.8%, 2.8%, 0.9% cells were sampled with 1, 2, 3, 4 ablation marks, respectively. To integrate

124 metabolic profiles from several ablation marks co-sampling the same cell as well as to reduce the

125 confusion of co-sampled cells, we developed a cell-ablation marks normalization strategy

126 (Figure 2). The normalization provides the metabolite intensity normalized by the area that is a

127 natural readout for metabolite concentration. Next, we developed a strategy to distinguish

128 intracellular from extracellular metabolites by requiring an intracellular metabolite intensities to

129 be highly correlated with the cell spatial distribution. Finally, similar to cell filtration strategies

130 in single-cell RNA-seq (Ilicic et al., 2016), we filter out poor-quality cells with low numbers of

131 metabolite annotations with the cutoff determined as the 5%-percentile of the numbers of

132 annotations for all cells in an experiment.

$$\text{normalized intensity} \ \text{Cell, } c_k = \frac{\sum\limits_{a_n} \text{intensity}(a_n) \cdot \dfrac{\text{area}(a_n)}{\text{sampling area}(a_n)} \cdot \dfrac{\text{area}(c_k) \cap \text{area}(a_n)}{\text{sampling area}(a_n)}}{\sum\limits_{a_n} \dfrac{\text{area}(c_k) \cap \text{area}(a_n)}{\text{sampling area}(a_n)}}$$

133

134 *Figure 2. Normalization strategy for assigning metabolic intensities to individual cells. The*

135 *intensity assigned to a cell for a given metabolite is calculated as a weighted mean of the*

136 *metabolite intensities from the ablation marks sampling that cell. To increase the contribution of*

137 *ablation marks which mainly sample the cell of interest, the weight of each ablation mark is*

138 *proportional to the overlap of the ablation mark and the cell. To reduce the contribution of*

139 *ablation marks which mainly sample extracellular areas, the weight of each ablation mark is*

140 *reversely proportional to its extracellular sampling area. Ablation marks sampling*

141 *predominantly extracellular areas are filtered out (as the illustrated here ablation mark III).*

8

142 *area(a_n) stands for the area of ablation mark a_n; sampling area(a_n) stands for the intracellular*

143 *area of ablation mark a_n; area(c_k) stands for the area of cell c_k; all areas are computed in*

144 *microscopy pixels.*

145 Ultimately, SpaceM provides a single-cell spatio-molecular matrix that, for each cell, comprises

146 a multiplex readout of the cell metabolic profile, fluorescence intensity, morphological features,

147 and spatial features (Figure 1). This information enables statistical analysis, phenotype-

148 metabolome correlation, and/or spatio-molecular interrogation of single cells in the genuine

149 spatial context.

150 **SpaceM predicts cell types with single-cell resolution**

151 For validation of the method, we evaluated whether SpaceM can predict the cell type of

152 spatially-heterogeneous co-cultured human HeLa cells and mouse NIH3T3 fibroblasts (Figure

153 3). We considered six samples (two replicates of co-cultures, and two replicates of control

154 monocultures for each cell type). HeLa and NIH3T3 cells constitutively expressed H2B-mCherry

155 and GFP, respectively, making them easily discernible by fluorescence microscopy. Automated

156 assignment of the cell type was done using a linear separating boundary between mCherry and

157 GFP fluorescence intensities (Figure 3A). Overall, metabolic profiles of 88 metabolites with an

158 FDR≤10% in at least one sample were obtained for 1624 cells in co-cultures (958 HeLa and 666

159 NIH3T3 cells) and 2197 cells in monocultures (1603 HeLa and 594 NIH3T3 cells). Support

160 Vector Machine classification of the single-cell metabolic profiles with the 10-fold cross-

161 validation for unbiased choice of the Gaussian kernel gamma predicted the cell type with 90.4%

162 accuracy for the co-cultured cells. To evaluate the richness of the detected metabolic profiles, we

163 used only a random subset of all 88 metabolites and were able to consistently predict the cell

164   type in co-cultures with 87.6% accuracy even when using only a half of all detected metabolites

165   (Figure 3B). This indicates the richness of the detected intracellular metabolomes and its

166   biological relevance in the context of cell type classification. Moreover, by applying the

167   statistical t-test we have identified the molecular markers of each cell type in co-cultures, with

168   the phosphatidylinositols PI(34:1), PI(34:2) found to be the most statistically significant and

169   exhibiting the highest fold change in HeLa cells.

170   In order to assess whether the metabolic profiles can predict the cell type with a single-cell

171   resolution, we evaluated a case of a fibroblast surrounded by HeLa cells (Figure 3D). As shown

172   in Figure 3E, its cell type was predicted correctly. The phosphoethanolamine PE(40:6), the

173   fibroblast marker for NIH3T3 with the highest fold change (Figure 3F) is exhibiting a higher

174   intensity in the fibroblast compared to the surrounding HeLa cells. Interestingly, the visualization

175   of the intensities of the most significant HeLa marker PI(34:1) shows high cell-cell heterogeneity

176   among the HeLa cells (Figure 3G), confirming that it is a combination of several metabolites that

177   enables prediction of the HeLa cell type.

178
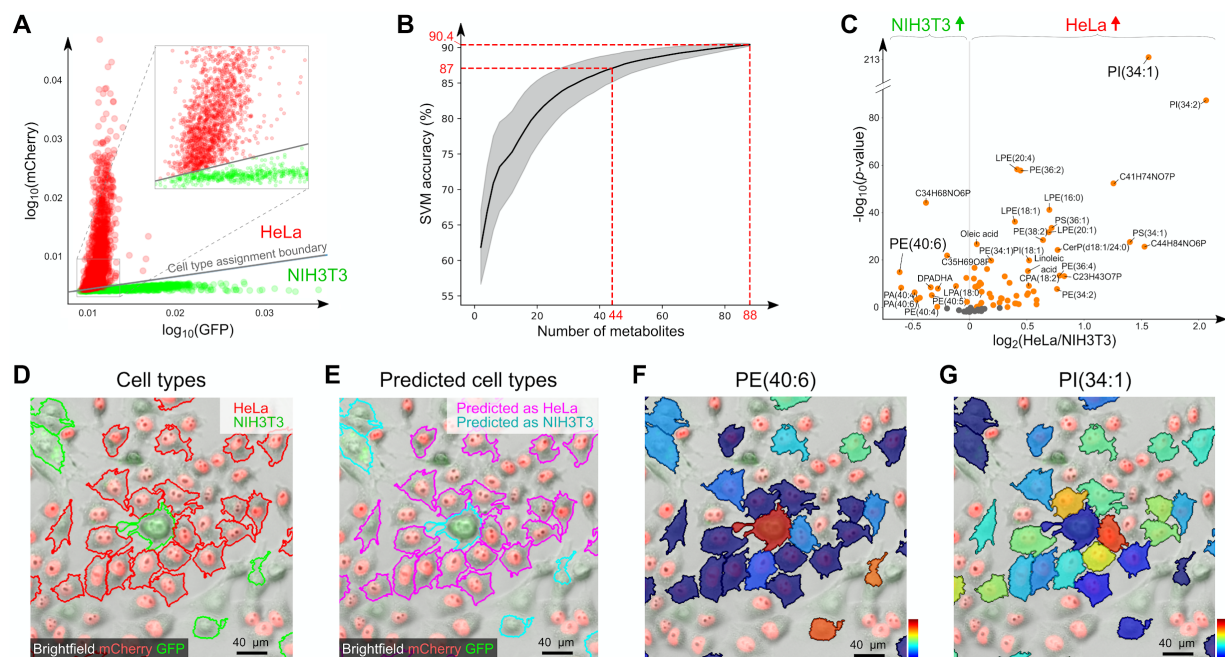
Figure 3. SpaceM can predict the cell type of co-cultured HeLa cells and NIH3T3 fibroblasts based on their intracellular metabolomes, with single-cell resolution. *A: Automated assignment of the cell type for co-cultured HeLa and NIH3T3 cells (n=3821) was done using a linear separating boundary between mCherry and GFP fluorescence intensities.* **B:** *Using single-cell metabolic profiles, we could predict the cell type with 90.4% accuracy; even when using only half of the detected metabolites, we could predict the cell type with 87.6% accuracy on average indicating the richness and the relevance of the detected metabolomes; Support Vector Machine with 10-fold cross validation was used for classification; the plot shows the median accuracy for 1000 random repetitions when subsampling the metabolites, with the grey area showing the confidence intervals of ± one standard deviation.* **C:** *Volcano plot (log2 of the fold change HeLa/NIH3T3 vs. -log10 of the t-test p-value) showing differential properties 88 detected metabolites and lipids.* **D:** *Area of the co-cultured cells showing an NIH3T3 cell surrounded by HeLa cells; the sampled cells are outlined according to their assigned type.* **E:** *SpaceM demonstrates single-cell resolution allowing correct prediction the cell type of the NIH3T3 cell*

11

193   *surrounded by HeLa cells. **F-G:** Single-cell metabolite images for two markers highlighted in*

194   *Figure 2E: phosphoethanolamine PE(40:6) and phosphatidylinositol PI(34:1) validated using*

195   *LC-MS/MS (Data S1); despite the single-cell metabolite images exhibiting visually-noticeable*

196   *heterogeneity, the full metabolic profile let predict the cell type with a high accuracy indicating*

197   *the richness of the detected metabolomes and their relevance for each cell type.*

198

199   **Intermixing of metabolomes of co-cultured HeLa and NIH3T3**

200   Intriguingly, the detected intracellular metabolomes of co-cultured cells were different from

201   metabolomes of their monocultured counterparts (Figure 4). The co-culturing was optimized to

202   achieve high spatial heterogeneity so that cells of one type have neighbors of another type

203   (Figure 4A-B). We observed that upon co-culturing, the single-cell metabolomes of one cell type

204   become more similar to the single-cell metabolomes of another cell type as compared to their

205   monocultured counterparts (Figure 4C). The values of the metabolic discriminant do not overlap

206   between the monocultured HeLa and NIH3T3 (Figure 4C, with the 90% confidence interval

207   shown monocultured cells of each type). However, for the co-cultured cells, 39.2% of NIH3T3

208   cells (and 48.2% of HeLa cells) exhibit the values of the metabolic discriminant in the mixing

209   region between the cell types or even take the values within the confidence interval of the other

210   type. This observation of metabolic intermixing between co-cultured cells was further supported

211   by results from predicting the cell type based on single-cell intracellular metabolomes. Whereas

212   we could predict the cell type of co-cultured cells with 90.4% accuracy, for the monocultured

213   cells we could predict their cell type with a higher accuracy of 96.6%.

214   Furthermore, we discovered that the metabolic intermixing between cells of two types happens

215   locally and can be considered a short-distance effect. The extent of the metabolic intermixing for

12

216   NIH3T3 cells depends on the presence of HeLa in their close vicinity (Figure 4D). We estimated

217   that the metabolic intermixing is the strongest at the distance of 58 μm for NIH3T3 and 107 μm

218   for HeLa, with NIH3T3 affected most (r_s=0.43, -log10(p-value)=17.5 compared to r_s=-0.18, -

219   log10(p-value)=3.8). We evaluated whether the observed metabolic intermixing can be observed

220   either due to metabolite delocalization during sample preparation or due to co-ablation of cells.

221   Sample preparation is known to be a key to achieve high spatial resolution MALDI-imaging.

222   Particularly critical is the application of the MALDI matrix, since it can cause metabolite

223   delocalization either during matrix crystallization as crystals can contain analytes from the whole

224   crystal footprint, or due to metabolite leakage while spraying the matrix solution. We have

225   developed a strategy to quantify metabolite delocalization (Figure 4G) that showed that most of

226   metabolites (65 of 88) are well-localized. The delocalized metabolites such as

227   lysophosphoethanolamine LPE(18:0) (see Figure G, cf. well-localized LPE(18:1)) showed only

228   minor levels of delocalization with median distance outside of cells <5 μm. Importantly, even

229   when using only well-localized metabolites, SpaceM could predict the cell type with 88.9%

230   accuracy. The fact that the cell type prediction accuracy did not increase after considering

231   localized metabolites only suggests that delocalization does not explain the observed intermixing

232   between the cell types. Next, we evaluated whether co-ablation of cells can be a reason for the

233   observed metabolic intermixing. We considered only the cells which had uniquely-associated

234   ablation marks and excluded 878 cells which were co-sampled (having co-sampling ablation

235   marks, Figure 4H). Still, considering both well-localized metabolites and cells without co-

236   sampling ablation marks only (444 HeLa, 332 NIH3T3) we could predict the cell type with

237   90.7% accuracy. The lack of the difference in the prediction accuracy (cf. 90.4% for all

238   metabolites and all cells) suggests that co-sampling of cells does not explain the observed

13

239 metabolic intermixing. In summary, this data indicates that the metabolic intermixing might be a

240 short-distance biological effect when a cell of one type has neighbors of another type in close

241 vicinity and that NIH3T3 cells are stronger affected than HeLa cells.
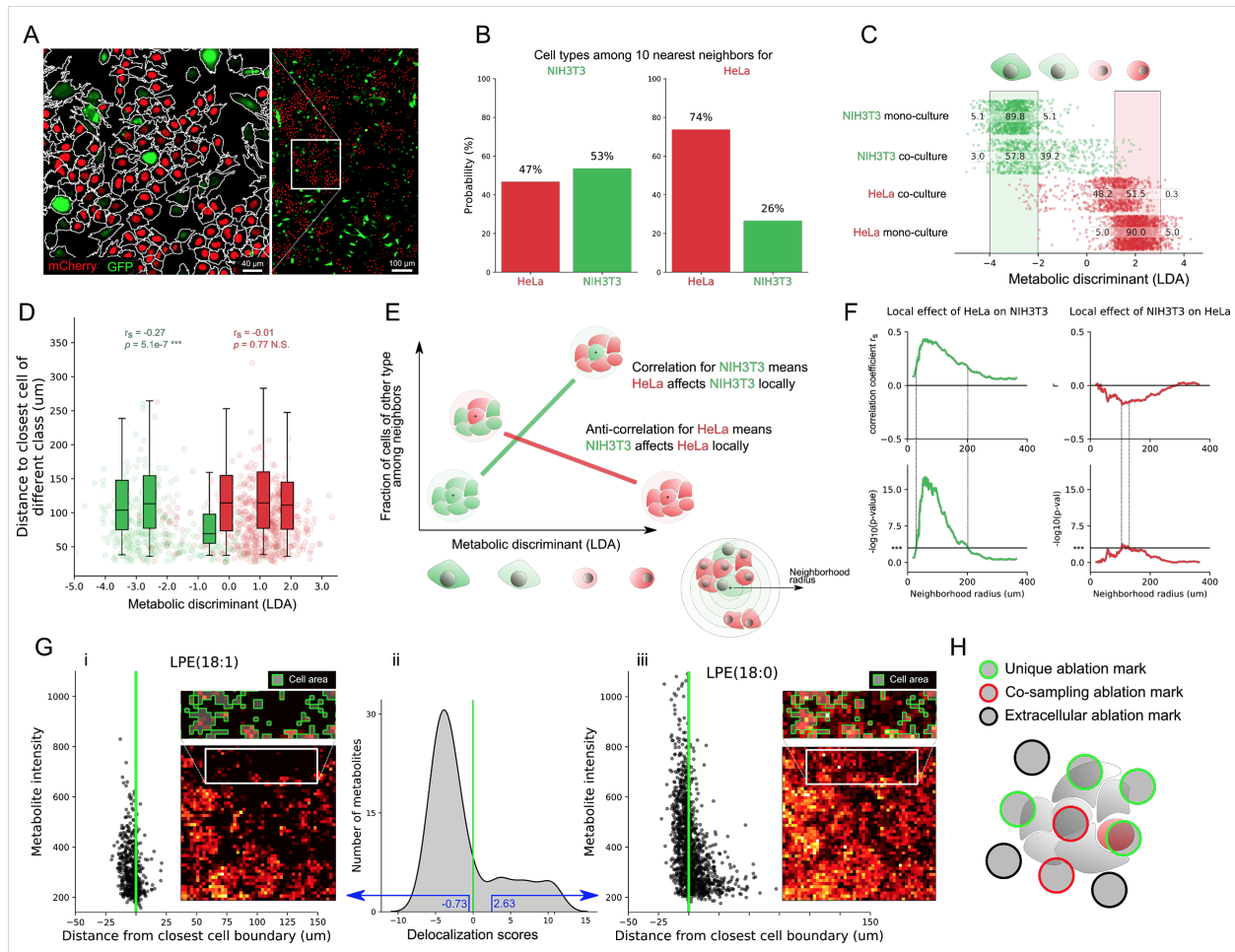
242

243 *Figure 4. Metabolic intermixing of co-cultured HeLa and NIH3T3 fibroblasts. A: Illustration*

244 *of the spatial heterogeneity of co-cultured HeLa (H1B-mCherry, red) and NIH3T3 (GFP, green).*

245 *B: Quantification of the spatial heterogeneity showing that, for each cell type, individual cells*

246 *are surrounded by cells of other type (on average, an NIH3T3 cell has 47% HeLa among 10*

247 *closest neighbors, a HeLa cell has 26% NIH3T3). C: Less pronounced difference between HeLa*

248 *and NIH3T3 cells in co-cultures compared to their monocultured counterparts suggests*

14

249 *metabolic intermixing between the cell types, here visualized with the values of the Linear*

250 *Discriminant Analysis (LDA) discriminant of the single-cell metabolic profiles; the cells are*

251 *colored and plotted against its cell type and whether they were cultured in co- or mono-culture;*

252 *the cell type for co-cultured cells was determined using their fluorescence; the vertical bars*

253 *indicate the 90%-confidence intervals for each monocultured cell type. **D:** The metabolomes of*

254 *NIH3T3 cells are affected most when they have HeLa cells in close vicinity with distance*

255 *between cell centers of 50-100 μm, whereas the average diameter of a HeLa cell equal to 6.7*

256 *(+/- 1.7) μm and of NIH3T3 equal to 8 (+/- 2.47) μm. **E:** Illustration explaining the calculation*

257 *of the distance of the metabolic intermixing effect, per cell type: For each cell, we consider a*

258 *neighborhood of particular radius, and calculate a fraction of cells of the other type in this*

259 *neighborhood. The radius for which this property is most correlated (for NIH3T3 cells) or anti-*

260 *correlated (for HeLa cells) with the metabolic discriminant (LDA) corresponds to the distance of*

261 *the intermixing effect. **F:** NIH3T3 cells are most affected by HeLa at the distance of 58 μm;*

262 *HeLa cells are mainly affected by NIH3T3 cells at the distance of 120 μm, with the correlation*

263 *coefficient and p-values indicating the smaller extend of this effect compared to NIH3T3. **G:***

264 *Evaluation of the metabolite delocalization confirmed that the metabolic intermixing cannot be*

265 *explained by the metabolite delocalization between neighboring cells. The scatterplots for*

266 *ablation marks for lysophosphoethanolamines LPE(18:1) (i) and LPE(18:0) (iii) show how their*

267 *metabolite intensities depend on the distance to the nearest cell boundary (negative for*

268 *intracellular ablation marks, positive for extracellular ablation marks). LPE(18:0) exemplifies a*

269 *delocalized metabolite with the high metabolite intensities observed at the extracellular ablation*

270 *marks at the distances of <50 μm from cells. LPE(18:1) exemplifies a well-localized metabolite*

271 *detected predominantly in the intracellular ablation marks only. ii) a histogram of the*

15

272   *delocalization scores for all metabolites showing that most of the metabolites are well-localized;*

273   *moreover, when considering only well-localized metabolites, SpaceM predicts the cell type with*

274   *the classification accuracy 88.9% suggesting that despite a minority of metabolites (23 out of 88)*

275   *having positive delocalization scores, the metabolic intermixing between the cell types is not*

276   *explained by the delocalization. **H:** We confirmed that the metabolic intermixing is not due to the*

277   *co-sampling of cells (when an ablation mark samples more than one cell e.g. as illustrated with*

278   *red outlines), since even after considering only well-localized metabolites and excluding co-*

279   *sampled SpaceM could predict the cell type with 90.7% accuracy (cf. 90.4% for all metabolites*

280   *and cells). *** denotes p-values<0.001; N.S. stands for non-significant.*

281   **SpaceM discovers accumulation of long-chain lipids in steatotic hepatocytes**

282   Next, we used SpaceM to investigate the identity of intracellular metabolomes in differentiated

283   human hepatocytes (dHepaRG). During the non-alcoholic fatty liver disease (NAFLD)

284   hepatocytes are known to accumulate lipid droplets (LDs), which in the context of inflammation

285   and necro-inflammation can lead to development of macrovesicular steatosis (Ringelhan et al.

286   2018; Wolf et al. 2014). We could recapitulate macrovesicular steatosis using human or murine

287   hepatocytes *in vitro* (Wolf et al. 2014). In particular, the pro-inflammatory cytokine TNFα is

288   known factor promoting steatotic phenotype in hepatocytes (Jung and Choi 2014; Nakagawa et

289   al. 2014). We noticed that the macrovesicular steatosis exhibits a high cell-cell heterogeneity

290   (Figure 5A, Figure S3) and set to characterize the molecular composition of the LDs in steatotic

291   hepatocytes.

292   We cultured monolayers of differentiated human hepatocytes dHepaRG, stimulated them with

293   TNFα in combination with oleic and palmitic acids, and measured LD accumulation using the

294   lipophilic fluorescent dye LD540 (Spandl et al., 2009). After applying SpaceM, we detected 167

295   metabolites (at an FDR≤10%) in 2370 cells. Principal component analysis (PCA) of the single-

296   cell metabolic profiles revealed a significant correlation between the captured metabolome and

297   the LD540 lipid fluorescence (Figure 5B). Triglycerides (TGs), diglycerides (DGs), and

298   phosphatidylcholines (PCs) were identified as the key constituents of the LDs (Figure 5C). This

299   is in line with neutral lipids, mainly DGs and TGs, known to compose the core of hepatic LDs,

300   whereas polar lipids, primarily PCs, to compose the surface (Gluchowski et al., 2017; Ress and

301   Kaser, 2016). Figure 5D shows a single-cell scatterplot for the most correlated lipid TG(50:1)

302   visualizing statistically significant (with p-value<0.001) correlation of intensities of this lipid

303   with the extent of the macrovesicular steatosis quantified with the LD540 fluorescence.

304   Interestingly, for PCs, sphingomyelins, and phosphoethanolamines, the LD540 fluorescence was

305   found to be positively correlated with the number of carbons suggesting that LDs in steatotic

306   hepatocytes preferentially accumulate long-chain species of these phospholipids (Figure 5E).

307   The opposite effect (negative correlation) was observed for di- and triglycerides albeit not

308   significant (Figure 5F).

309
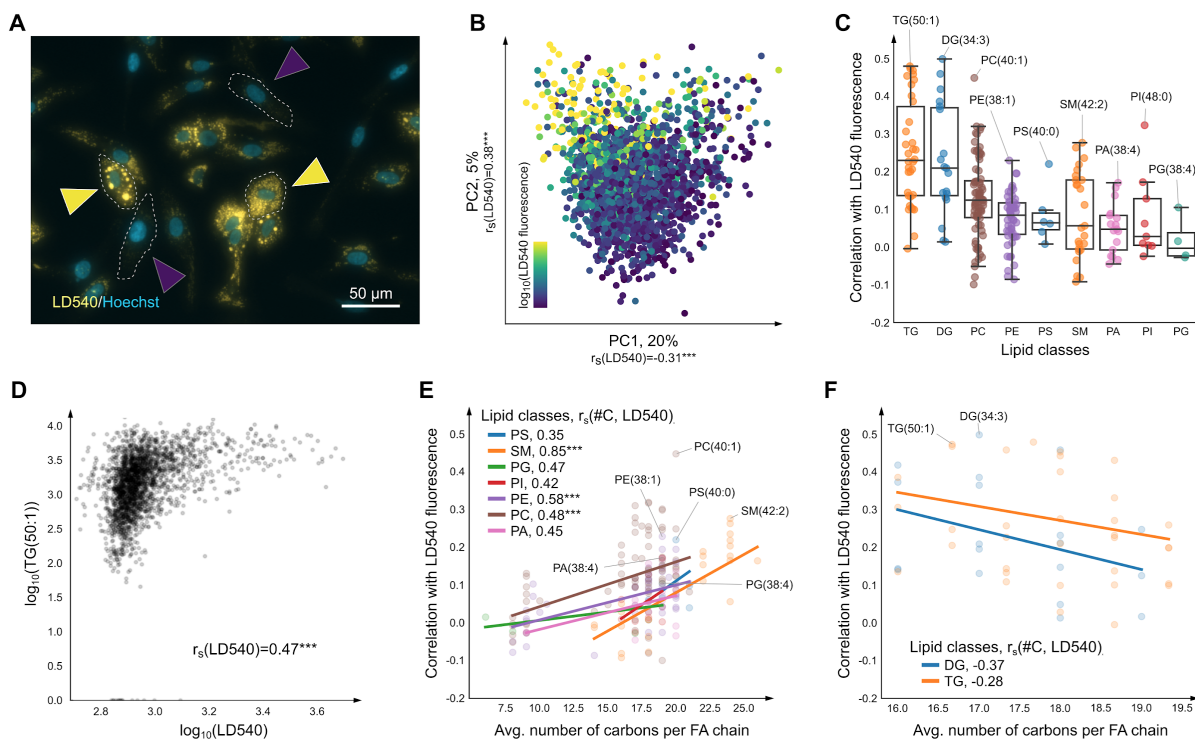
Figure 5. Single-cell analysis of the molecular composition of lipid droplets (LDs) in steatotic

hepatocytes stimulated with TNFα (n=2370). A: *Cell-cell heterogeneity of macrovesicular*

steatosis (LDs accumulation) in differentiated human hepatocytes stimulated with TNFα in

combination with oleic and palmitic fatty acids; the LD540 lipophilic staining highlights

intracellular lipid droplets; Hoechst highlights nuclei; the yellow/blue arrows indicate cells with

high/low steatosis. ***B:*** *Positive Spearman correlations (rₛ) the single-cell principal components*

of the z-scores of the single-cell metabolic profiles between the log10 of LD540 fluorescence

prove that the metabolic profiles represent lipid accumulation. ***C:*** *Accumulation of various lipid*

classes in LDs as measured by the single-cell Spearman correlations between LD540

fluorescence and intensities of 167 detected lipid species; tri- (TG), di-glycerides (DG), and

phosphocholines (PC) are the most correlated that is in line with them known to compose the

core (TG, DG) and surface (PC) of hepatic LDs. ***D:*** *Single-cell scatterplot of the most-correlated*

triglyceride TG(50:1), validated using LC-MS/MS (Data S1). ***E:*** *For phosphocholines,*

18

323 *sphingomyelins (SMs), and phosphoethanolamines (PEs), the LD540 fluorescence is*

324 *significantly and positively correlated with the number of carbons (#C) suggesting that steatotic*

325 *hepatocytes accumulate long-chain versions of these phospholipids; the number of carbons is*

326 *computed as an average per fatty acid chain to be comparable between lipid classes. **F:** The*

327 *opposite effect (negative correlation) was observed for di- and triglycerides albeit not*

328 *significant. *** indicates significance with p-value ≤ 0.001.*

329 **SpaceM discovers intracellular co-regulation of oleic and linoleic acid**

330 We previously found that mice fed a diet enriched with oleic and palmitic fatty acids developed

331 key features of human metabolic syndrome, nonalcoholic steatohepatitis (NASH), and NASH-

332 derived hepatocellular carcinoma (Wolf et al., 2014). To investigate on the single-cell level how

333 the metabolome and lipidome of human hepatocytes is affected by different pro-inflammatory

334 factors, we analyzed hepatocytes cultured under the following conditions: (i) CTRL, untreated

335 cells, (ii) FA, cells stimulated with oleic and palmitic fatty acids (opFAs), (iii) LPS, cells

336 stimulated with a pathogen-associated molecular pattern lipopolysaccharide and opFAs and (iv)

337 TNFα, cells stimulated with TNFα and opFAs. SpaceM obtained metabolic profiles of 136

338 metabolites for 22258 cells in total with a batch correction applied to three randomized technical

339 replicates per condition (Table S1, Figure S4). LD540 staining of differentiated, stimulated

340 human hepatocytes revealed lipid accumulation and macrovesicular steatosis (Figs. 5A, S6, S8).

341 PCA of single-cell metabolic profiles indicates the captured differences in the metabolomes of

342 untreated and stimulated cells (Figure 6A). The metabolic shifts between different conditions

343 reflected the expected levels of response to the stimuli as (i) opFAs used for stimulation in the

344 FA condition were also supplemented in the LPS and TNF condition, (ii) TNFα specifically

345 induced the strongest TNF-receptor signaling whereas (iii) LPS only secondarily induces TNF

346   secretion and TNFR signaling at lower levels (Beutler, 2004). We investigated the contributions

347   of individual metabolites to the principal components and found that, as expected, cells cultured

348   with oleic acid accumulated intracellular oleic acid as compared to the untreated cells (Figure

349   6B). Not all molecules showed elevated accumulation with the increase of the stimuli; see e.g.

350   PIP(38:5) in Figure 4C which exhibits similar intensities between CTRL and FA with a clear

351   increase in the TNF and even more in the LPS condition. Interestingly, opposite to oleic acid,

352   linoleic acid (the second of the opFAs stimuli in the FA, LPS, TNF conditions) exhibits

353   decreased levels in the stimulated cells (Figure 6D). Importantly, there is a clear correlation

354   between the levels of the oleic and linoleic acids across all cells (Figure 6E). A similar effect of

355   the inverse relation between oleic and linoleic acids levels was reported in the livers of mice fed

356   a high-fat diet (da Silva-Santi et al., 2016). However, the bulk analysis could not discern whether

357   the effect occurs in different cell subpopulations or is concerted within the same cells. Our

358   single-cell analysis shows that the effect happens indeed within the same cells thus suggesting

359   intracellular co-regulation of oleic and linoleic acid levels.

360
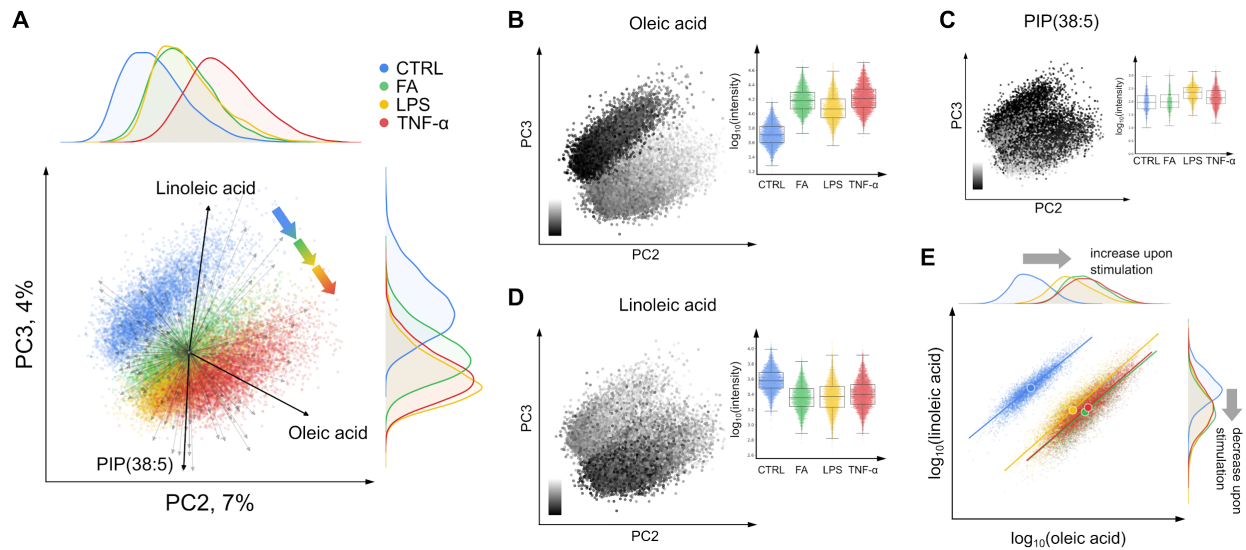
***Figure 6. Single-cell statistical analysis of steatotic differentiated human hepatocytes dHepaRG stimulated with the fatty acids, LPS, and TNFα (n=22258). A:** PCA of z-scores of the single-cell profiles of 136 metabolites; biplot vectors visualize contributions of individual metabolites; gradient-colored arrows illustrate the metabolomes transitions from the untreated cells (CTRL, n=5654) to the cells cultured with oleic and palmitic fatty acids (FA, n=4972), with LPS and the fatty acids (LPS, n=5062), or with TNFα and the fatty acids (TNFα, n=6570). **B-D:** Single-cell metabolite intensities mapped onto the PCA plot and the Tukey box plots per condition (25%-75% percentiles, whiskers at 1.5x distance of the interquartile range); only cells with non-zero metabolite intensity are shown; see Figure 14 for AMP and glutathione. **E:** Single-cell scatterplot for intensities of linoleic vs. oleic acids showing an inverse relationship in intracellular levels of these fatty acids upon stimulation and their tight and condition-independent correlation; the centers of masses and fitted lines are plotted. Oleic acid, linoleic acid, and PIP(38:5) were validated using LC-MS/MS (Data S1).*

21

377   **SpaceM discovers association of PIP(38:5) with high cell-cell contact**

378   Finally, we investigated the spatio-molecular organization of human hepatocytes (Figure 7A-D).

379   LD540-fluorescence microscopy revealed lipid accumulation within groups of cells that display

380   high cell-cell contact (Figure S5, S6). Among all the detected metabolites, phosphatidylinositol

381   phosphate PIP(38:4) (although not validated with LC-MS/MS) and PIP(38:5) were most highly

382   associated with cell-cell contact (Figure 7B, Figure S7). PIPs are precursors of PIP3, a signaling

383   phospholipid in the plasma membrane, which might explain their elevation within adjacent cells

384   in a locally-concerted manner. Not all detected metabolites displayed such an association: AMP

385   showed no correlation (Figure 7C) whereas oleic acid showed a negative correlation (Figure 7D).

386   Thus, integrating fluorescent, morphological, spatial, and molecular information can be a

387   powerful approach to explore multi-cellular phenomena (Bray et al., 2016).

388

22
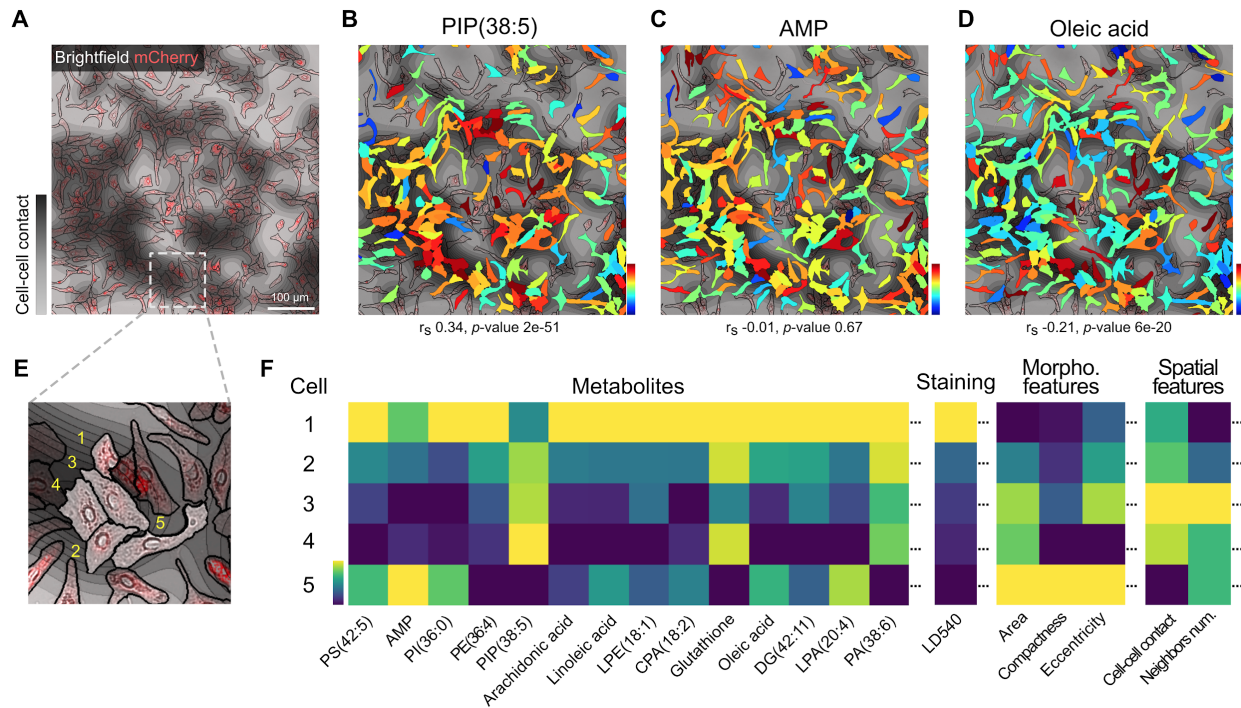
Figure 7. Single-cell statistical analysis of steatotic differentiated human hepatocytes stimulated with pro-inflammatory factors (n=22258). A: TNFα hepatocytes with areas of local crowding; the red LD540 fluorescence intensity indicates the accumulation of lipid droplets from low steatosis to macrovesicular steatosis. B-D: Single-cell molecular images for PIP(38:5), AMP, and oleic acid. Next to PIP(38:4), PIP(38:5) is the second most correlated molecule with cell-cell contact, indicating its potential concerted elevation within adjacent cells. Oleic acid, linoleic acid, AMP, glutathione, and PIP(38:5) were validated using LC-MS/MS (Data S1). E-F: Illustration of a part of spatio-molecular matrix for five selected cells that represents single-cell phenotypic information (LD540 fluorescence quantifying the extent of the macrovesicular steatosis), morpho-spatial features (including cell-cell contact), and metabolite intensities.

23

Discussion

400

401 Here, we presented SpaceM, a novel method for the spatial single-cell analysis of intracellular

402 metabolomes of cultured cells. SpaceM not only detects metabolites in individual cells using

403 MALDI but, critically, integrates MALDI analysis with microscopy and is supplied with data

404 analysis strategies for metabolite annotation, intensities normalization, selection intracellular

405 metabolites and filtering out poor quality cells. The method demonstrated to be robust and

406 reproducible, allowing us to analyze several conditions and replicates, obtaining metabolic

407 profiles of around 100 metabolites from over 30.000 cells.

408 We benchmarked the method by analysing the co-cultured human HeLa cells and mouse

409 NIH3T3 fibroblasts. The single-cell metabolic profiles detected by SpaceM were rich enough to

410 predict the cell type with 90.4% accuracy with the single-cell resolution. Surprisingly, we

411 detected metabolic intermixing of different cell types upon co-culturing, a yet unreported

412 biological phenomenon. Our investigations indicated that the observed intermixing is a short-

413 distance effect, namely, its extent depends on the presence of cells of other type in close vicinity.

414 We carefully considered all other confounding factors and outruled sampling inaccuracies or

415 metabolite delocalization. All our results indicate that intracellular metabolomes of cells of one

416 type are indeed influenced by the neighboring cells of another type, with NIH3T3 cells affected

417 stronger than HeLa cells.

418 For molecular detection, SpaceM exploits MALDI-imaging thus inheriting the advantages of this

419 technique, in particular the capacity for untargeted metabolomics. We demonstrated it by

420 detecting profiles encompassing 88 (for HeLa and NIH3T3) and 136 (for dHepaRG) metabolite

421 annotations on the level 2 according to the Metabolomics Standards Initiative (Sumner et al.,

24

422   2007). The use of METASPACE for metabolite annotation was instrumental in the

423   interpretation, quality control, and fast access to the metabolite images of the collected MALDI-

424   imaging data, as METASPACE efficiently reduces millions of mass-to-charge values to tens of

425   metabolite annotations in a False Discovery Rate-controlled manner. SpaceM is not limited to

426   lipids, fatty acids and such small molecules as AMP or glutathione (Figure S8, Data S1) but can

427   be extended to other molecular classes by using another MALDI-imaging protocol. In the HeLa-

428   NIH3T3 co-culture benchmarking experiment, even when using just a half of the 88 detected

429   metabolites, we could predict the cell type with 87.6% accuracy that affirms the richness of the

430   metabolic profiles detected by SpaceM.

431   SpaceM was enabled by MALDI-imaging achieving the single-cell spatial resolution. However,

432   it is almost impossible to sample highly-confluent cell monolayers without co-ablating several

433   cells at once. Moreover, the sample preparation for MALDI-imaging, particularly matrix

434   application, can negatively affect the spatial resolution. Thus, we set to prove the single-cell

435   nature of the method, especially because it was essential to exclude possible technical reasons for

436   the observed metabolic intermixing between HeLa and NIH3T3. For this, we developed a

437   strategy to consider for each metabolite its delocalization outside the cell perimeter. This led to

438   revelation that, first, the extent of delocalization is metabolite-specific, and second, even for the

439   minority of metabolites characterized as delocalized, the median delocalization is comparable to

440   the average size of a single cell. Moreover, in our benchmarking experiment, discarding

441   delocalized metabolites did not affect the accuracy of the cell type prediction much. Altogether,

442   these novel delocalization analyses confirm the single-cell nature of the SpaceM method. We

443   hypothesize that the delocalization happens during spraying the MALDI matrix solution but do

444   not have yet a definite answer what makes some metabolites delocalized while the majority of

445   metabolites were detected well-localized within the cell perimeter. For example,

446   lysophosphoethanolamine LPE(18:1) was found to be well-localized whereas the structurally

447   similar but saturated LPE(18:0) was found to be delocalized.

448   Compared to other reported single-cell metabolomics methods, e.g. microwells (Ibáñez et al.,

449   2013) or microsampling (Guillaume-Gentil et al., 2017) approaches, SpaceM analyzes cells *in*

450   *situ* in their native spatial context, ensures minimal unwanted perturbation, and preserves

451   information about the microenvironment and spatial organization of cells. In contrast to micro-

452   and nano-sampling methods, SpaceM is also a high-throughput method able to analyze over

453   10000 cells and at the same time, as we illustrated, detecting rich metabolic profiles. Compared

454   to a microscopy-guided laser ablation approach (Do et al., 2017), SpaceM uses unbiased

455   sampling that facilitates discovery of cell populations which cannot be discriminated by

456   microscopy, helps distinguish intracellular from extracellular signals, and also capitalizes on a

457   softer MALDI ionization better suited for biomolecules. Compared to ultra-high spatial

458   resolution approaches (Passarelli et al., 2017), SpaceM makes possible a high throughput

459   analysis of large populations of cells to investigate their heterogeneity and to discover rare

460   molecular phenotypes. The combination of these strengths makes SpaceM not only a single-cell

461   but also a spatial method. We demonstrated the spatial capacity of SpaceM by discovering short-

462   distance effect of metabolic intermixing between HeLa and NIH3T3 cells and by associating

463   PIPs with high cell-cell contact.

464   We expect SpaceM to be broadly applicable to any adherent cells cultured in a monolayer,

465   avoiding growing on top of each other that can lead to increased co-sampling. In our experience,

466   cell culturing for SpaceM is relatively straightforward and can be evaluated following

467   conventional cell biology practices by paying attention to the cell count, viability and

468   confluence. SpaceM allows for the determination of cells that are different in their response to

469   changes in the microenvironment, which enables the identification of novel molecular

470   mechanism involved in critical biological processes.

471   SpaceM contributes to the growing field of single-cell -omics methods by providing the missing

472   capacities for spatio-molecular *in situ* analysis. Future experiments will aim to translate SpaceM

473   to the level of tissue sections. Our method will be particularly useful to investigate health and

474   disease phenomena associated with metabolic reprogramming, spatial organization and/or

475   cellular heterogeneity such as differentiation, infection, drug metabolism, immunity, and cancer.

Acknowledgements

489 M.S.), Darwin Trust of Edinburgh (S.T.), SFB Transregio grants 179, 209, and 1335 (all M.H.),

490 and the ERC Consolidator grants HepatoMetaboPath (M.H.) and METACELL (T.A.).

Author Contributions

492 L.R. and T.A. conceived the research. L.R. developed the method. T.A. supervised the study.

493 S.T. performed the co-culture experiment. P.P. performed LC-MS/MS validation. M.S. and M.H.

494 contributed with the hepatocytes model, conceived the treatment design. M.S. cultured and

495 prepared hepatocytes. L.R., M.S., M.H. and T.A. interpreted data. L.R. and T.A. wrote the paper.

496 M.S. and M.H. contributed to the paper writing.

Declaration of Interests

498 L.R. and T.A. are the inventors on a patent application describing a spatial single-cell

499 metabolomics method. T.A. is a consultant and a member of the scientific advisory board of

500 SCiLS, a Bruker company developing software for MALDI-imaging.

501

502

503

References

Altschuler, S.J., and Wu, L.F. (2010). Cellular heterogeneity: do differences make a difference? Cell *141*, 559–563.

Baker, T.C., Han, J., and Borchers, C.H. (2017). Recent advancements in matrix-assisted laser desorption/ionization mass spectrometry imaging. Curr. Opin. Biotechnol. *43*, 62–69.

Beutler, B. (2004). Inferences, questions and possibilities in Toll-like receptor signalling. Nature *430*, 257–263.

Bray, M.-A., Singh, S., Han, H., Davis, C.T., Borgeson, B., Hartland, C., Kost-Alimova, M., Gustafsdottir, S.M., Gibson, C.C., and Carpenter, A.E. (2016). Cell Painting, a high-content image-based assay for morphological profiling using multiplexed fluorescent dyes. Nat. Protoc. *11*, 1757–1774.

Buck, M.D., Sowell, R.T., Kaech, S.M., and Pearce, E.L. (2017). Metabolic Instruction of Immunity. Cell *169*, 570–586.

Carpenter, A.E., Jones, T.R., Lamprecht, M.R., Clarke, C., Kang, I.H., Friman, O., Guertin, D.A., Chang, J.H., Lindquist, R.A., Moffat, J., et al. (2006). CellProfiler: image analysis software for identifying and quantifying cell phenotypes. Genome Biol. *7*, R100.

Do, T.D., Comi, T.J., Dunham, S.J.B., Rubakhin, S.S., and Sweedler, J.V. (2017). Single Cell Profiling Using Ionic Liquid Matrix-Enhanced Secondary Ion Mass Spectrometry for Neuronal Cell Type Differentiation. Anal. Chem. *89*, 3078–3086.

Folch, J., Lees, M., and Sloane Stanley, G.H. (1957). A simple method for the isolation and purification of total lipides from animal tissues. J. Biol. Chem. *226*, 497–509.

Fortin, J.-P., Cullen, N., Sheline, Y.I., Taylor, W.D., Aselcioglu, I., Cook, P.A., Adams, P., Cooper, C., Fava, M., McGrath, P.J., et al. (2017). Harmonization of cortical thickness measurements across scanners and sites. Neuroimage *167*, 104–120.

Gluchowski, N.L., Becuwe, M., Walther, T.C., and Farese, R.V., Jr (2017). Lipid droplets and liver disease: from basic biology to clinical implications. Nat. Rev. Gastroenterol. Hepatol. *14*, 343–355.

Gripon, P., Rumin, S., Urban, S., Le Seyec, J., Glaise, D., Cannie, I., Guyomard, C., Lucas, J., Trepo, C., and Guguen-Guillouzo, C. (2002). Infection of a human hepatoma cell line by hepatitis B virus. Proc. Natl. Acad. Sci. U. S. A. *99*, 15655–15660.

Grün, D., and van Oudenaarden, A. (2015). Design and Analysis of Single-Cell Sequencing Experiments. Cell *163*, 799–810.

Guillaume-Gentil, O., Rey, T., Kiefer, P., Ibáñez, A.J., Steinhoff, R., Brönnimann, R., Dorwling-

537 Carter, L., Zambelli, T., Zenobi, R., and Vorholt, J.A. (2017). Single-Cell Mass Spectrometry of
538 Metabolites Extracted from Live Cells by Fluidic Force Microscopy. Anal. Chem. *89*, 5017–
539 5023.

540 Ibáñez, A.J., Fagerer, S.R., Schmidt, A.M., Urban, P.L., Jefimovs, K., Geiger, P., Dechant, R.,
541 Heinemann, M., and Zenobi, R. (2013). Mass spectrometry-based metabolomics of single yeast
542 cells. Proc. Natl. Acad. Sci. U. S. A. *110*, 8790–8794.

543 Ilicic, T., Kim, J.K., Kolodziejczyk, A.A., Bagger, F.O., McCarthy, D.J., Marioni, J.C., and
544 Teichmann, S.A. (2016). Classification of low quality cells from single-cell RNA-seq data.
545 Genome Biol. *17*, 29.

546 Jung, U.J., and Choi, M.-S. (2014). Obesity and its metabolic complications: the role of
547 adipokines and the relationship between obesity, inflammation, insulin resistance, dyslipidemia
548 and nonalcoholic fatty liver disease. Int. J. Mol. Sci. *15*, 6184–6223.

549 Lee, M.-C.W., Lopez-Diaz, F.J., Khan, S.Y., Tariq, M.A., Dayn, Y., Vaske, C.J., Radenbaugh,
550 A.J., Kim, H.J., Emerson, B.M., and Pourmand, N. (2014). Single-cell analyses of transcriptional
551 heterogeneity during drug tolerance transition in cancer cells by RNA sequencing. Proc. Natl.
552 Acad. Sci. U. S. A. *111*, E4726–E4735.

553 Marioni, J.C., and Arendt, D. (2017). How Single-Cell Genomics Is Changing Evolutionary and
554 Developmental Biology. Annu. Rev. Cell Dev. Biol. *33*, 537–553.

555 Merrill, C.B., Basit, A., Armirotti, A., Jia, Y., Gall, C.M., Lynch, G., and Piomelli, D. (2017).
556 Patch clamp-assisted single neuron lipidomics. Sci. Rep. *7*, 5318.

557 Murphy, M.P., and O'Neill, L.A.J. (2018). Krebs Cycle Reimagined: The Emerging Roles of
558 Succinate and Itaconate as Signal Transducers. Cell *174*, 780–784.

559 Otsu, N. (1979). A threshold selection method from gray-level histograms. IEEE Trans. Syst.
560 Man Cybern. *9*, 62–66.

561 Palmer, A., Trede, D., and Alexandrov, T. (2016). Where imaging mass spectrometry stands:
562 here are the numbers. Metabolomics *12*, 1–3.

563 Palmer, A., Phapale, P., Chernyavsky, I., Lavigne, R., Fay, D., Tarasov, A., Kovalev, V.,
564 Fuchser, J., Nikolenko, S., Pineau, C., et al. (2017). FDR-controlled metabolite annotation for
565 high-resolution imaging mass spectrometry. Nat. Methods *14*, 57–60.

566 Passarelli, M.K., Pirkl, A., Moellers, R., Grinfeld, D., Kollmer, F., Havelund, R., Newman, C.F.,
567 Marshall, P.S., Arlinghaus, H., Alexander, M.R., et al. (2017). The 3D OrbiSIMS-label-free
568 metabolic imaging with subcellular lateral resolution and high mass-resolving power. Nat.
569 Methods *14*, 1175–1183.

570 Patel, A.P., Tirosh, I., Trombetta, J.J., Shalek, A.K., Gillespie, S.M., Wakimoto, H., Cahill, D.P.,
571 Nahed, B.V., Curry, W.T., Martuza, R.L., et al. (2014). Single-cell RNA-seq highlights
572 intratumoral heterogeneity in primary glioblastoma. Science *344*, 1396–1401.

573 Pavlova, N.N., and Thompson, C.B. (2016). The Emerging Hallmarks of Cancer Metabolism.
574 Cell Metab. *23*, 27–47.

575 Pelkmans, L. (2012). Cell Biology. Using cell-to-cell variability--a new era in molecular biology.
576 Science *336*, 425–426.

577 Preibisch, S., Saalfeld, S., and Tomancak, P. (2009). Globally optimal stitching of tiled 3D
578 microscopic image acquisitions. Bioinformatics *25*, 1463–1465.

579 Protsyuk, I., Melnik, A.V., Nothias, L.-F., Rappez, L., Phapale, P., Aksenov, A.A., Bouslimani,
580 A., Ryazanov, S., Dorrestein, P.C., and Alexandrov, T. (2018). 3D molecular cartography using
581 LC-MS facilitated by Optimus and 'ili software. Nat. Protoc. *13*, 134–154.

582 Ress, C., and Kaser, S. (2016). Mechanisms of intrahepatic triglyceride accumulation. World J.
583 Gastroenterol. *22*, 1664–1673.

584 Rubakhin, S.S., Lanni, E.J., and Sweedler, J.V. (2013). Progress toward single cell
585 metabolomics. Curr. Opin. Biotechnol. *24*, 95–104.

586 Russell, A.B., Trapnell, C., and Bloom, J.D. (2018). Extreme heterogeneity of influenza virus
587 infection in single cells. Elife *7*.

588 Sharma, U., and Rando, O.J. (2017). Metabolic Inputs into the Epigenome. Cell Metab. *25*, 544–
589 558.

590 Sharon, G., Garg, N., Debelius, J., Knight, R., Dorrestein, P.C., and Mazmanian, S.K. (2014).
591 Specialized metabolites from the microbiome in health and disease. Cell Metab. *20*, 719–730.

592 da Silva-Santi, L.G., Antunes, M.M., Caparroz-Assef, S.M., Carbonera, F., Masi, L.N., Curi, R.,
593 Visentainer, J.V., and Bazotte, R.B. (2016). Liver Fatty Acid Composition and Inflammation in
594 Mice Fed with High-Carbohydrate Diet or High-Fat Diet. Nutrients *8*.

595 Soltwisch, J., Kettling, H., Vens-Cappell, S., Wiegelmann, M., Müthing, J., and Dreisewerd, K.
596 (2015). Mass spectrometry imaging with laser-induced postionization. Science *348*, 211–215.

597 Spandl, J., White, D.J., Peychl, J., and Thiele, C. (2009). Live cell multicolor imaging of lipid
598 droplets with a new dye, LD540. Traffic *10*, 1579–1584.

599 Sumner, L.W., Amberg, A., Barrett, D., Beale, M.H., Beger, R., Daykin, C.A., Fan, T.W.-M.,
600 Fiehn, O., Goodacre, R., Griffin, J.L., et al. (2007). Proposed minimum reporting standards for
601 chemical analysis Chemical Analysis Working Group (CAWG) Metabolomics Standards
602 Initiative (MSI). Metabolomics *3*, 211–221.

603 Wellen, K.E., and Thompson, C.B. (2012). A two-way street: reciprocal regulation of
604 metabolism and signalling. Nat. Rev. Mol. Cell Biol. *13*, 270–276.

605 Wishart, D.S., Knox, C., Guo, A.C., Eisner, R., Young, N., Gautam, B., Hau, D.D., Psychogios,
606 N., Dong, E., Bouatra, S., et al. (2009). HMDB: a knowledgebase for the human metabolome.

607   Nucleic Acids Res. *37*, D603–D610.

608   Wolf, M.J., Adili, A., Piotrowitz, K., Abdullah, Z., Boege, Y., Stemmer, K., Ringelhan, M.,
609   Simonavicius, N., Egger, M., Wohlleber, D., et al. (2014). Metabolic activation of intrahepatic
610   CD8+ T cells and NKT cells causes nonalcoholic steatohepatitis and liver cancer via cross-talk
611   with hepatocytes. Cancer Cell *26*, 549–564.

612   Zenobi, R. (2013). Single-cell metabolomics: analytical and biological perspectives. Science
613   *342*, 1243259.

614

Methods

615

Co-culturing of HeLa and NIH3T3 cells

616

617 HeLa Kyoto H2B-mCherry and NIH3T3-GFP cells were cultured at 37 °C with 5% CO2, and

618 were maintained in high glucose DMEM (1X Pen/Strep) (Gibco/ThermoFisher Scientific,

619 Bremen, Germany) supplemented with 10% FBS, 100 U/ml penicillin, 100 μg/ml streptomycin

620 (Gibco) and 1 mM sodium pyruvate (Gibco). Cells were trypsinized with 0.25% trypsin-EDTA

621 (Gibco) and split 1:10 twice a week. Two technical replicates for the co-cultures and one

622 replicate for monoculture were used. Trypsinized cells were counted and cells were seeded on 4-

623 well-glass labtek chamber slides (Lab-Tek II, CC2) (ThermoFisher Scientific). In the co-culture

624 experiment, equal number of cells of each cell type was added into each well ($4x10^5$ cells/well).

625 After 48h of incubation cells were washed with PBS. After washing, the cells were fixed for 15

626 min with 4% paraformaldehyde (Sigma Aldrich, Darmstadt, Germany) at room temperature.

627 Then the cells were stained with DAPI (1μg/ml) (ThermoFisher Scientific) in PBS for 20 min at

628 room temperature.

Hepatocytes culturing and stimulation

629

630 HepaRG cell culture and differentiation was performed as described earlier (Gripon et al., 2002).

631 Differentiated HepaRG (dHepaRG) cells were cultured on 4-well-glass chamber slides (Lab-Tek

632 II, CC2, ThermoFisher Scientific, Bremen, Germany) ($5.5x10^4$ cells/well). The cells were

633 stimulated with the fatty acids (opFAs): oleic acid (66 μM) and palmitic acid (33 μM), opFAs

634 and tumor necrosis-alpha (TNFα) with the final concentration of 50 ng/ml (Recombinant Human

635 TNF-alpha, and Systems), or opFAs and lipopolysaccharide (LPS) (100 ng/ml) (LPS from

636 *E.coli*) (Sigma Aldrich) in Williams E Medium (William's Medium E, with stab. glutamine,

637   without Phenol Red, with 2,24 g/l NaHCO3) (PAN Biotech) for 24 h. Cells grown in Williams E

638   Medium without supplement for 24 h were considered as a negative control. For each of those

639   four conditions, cells were seeded in three different wells which were considered as technical

640   replicates (Table S1). After washing, cells were fixed for 15 min with 4% paraformaldehyde

641   (Sigma Aldrich) at room temperature. Then the cells were washed and stained with Hoechst

642   (1µg/ml) (Hoechst 33342) (ThermoFisher Scientific) and LD540 (0.1 µg/ml) (Spandl et al.,

643   2009) in PBS for 30 min at room temperature. After washing, cells were stored in dH2O at 4 °C

644   for one night maximum.

645   **Preparing cells for imaging**

646   The plastic walls of the labtek were removed and the cells were dried in a Lab Companion™

647   Cabinet Vacuum Desiccator for 16h at room temperature and -0.08 MPa. After complete

648   desiccation of the cells, pen marks are manually drawn on the glass slide using a black alcohol

649   pen model 140s black (Edding, Ahrensburg, Germany) to keep track of the glass slide orientation

650   and for image registration. The marks were drawn on the same side as the cells. Cells are kept at

651   4 °C until analysis. For the following experiments, the samples were analyzed by the microscopy

652   and MALDI-imaging mass spectrometry following a randomized experimental design (Table

653   S1).

654

655

656   **Pre-MALDI bright-field and fluorescence microscopy of cells**

657   Fixed cells were sequentially observed with the camera Nikon DS-Qi2 (Nikon Instruments) with

658   the Plan Fluor 10x (NA 0.30) objective (Nikon Instruments) mounted on the Nikon Ti-E inverted

34

659   microscope (Nikon Instruments) in bright-field and fluorescence (620 nm and 460 nm). The

660   pixel size was 0.73 μm. The microscope was controlled using the Nikon NIS Elements software.

661   The tiled acquisition of each cell culture area was performed using the JOB functionality of the

662   NIS software. Stitching of tiled frames was performed using the FIJI stitching plugin (Preibisch

663   et al., 2009).

664   **MALDI imaging mass spectrometry**

665   Relative humidity and temperature levels in the mass spectrometry room were monitored and

666   controlled during the whole experiment and were within 44%-63% and 21.1-23.7 °C (Table S1).

667   For the analysis of the lipid droplets (Figure 3), the 2,5-dihydroxybenzoic acid (DHB) matrix

668   (Sigma Aldrich) 15mg/ml dissolved in 70% acetonitrile was applied onto the dried cells on the

669   labtek slides by using a TM-Sprayer robotic sprayer (HTX Technologies, Carrboro, NC, USA).

670   Spraying parameters were as following: temperature=100 °C, number of passes=8, flow

671   rate=0.07 ml/min, velocity=1350 mm/min, track spacing=2 mm/min, pattern=CC, pressure=10

672   psi, gas flow rate=5 l/min, drying time=15 sec, nozzle height=41 mm. The estimated matrix

673   density was of 0.00311 mg/mm^2. For investigating the molecular trends within all four

674   considered conditions (Figure 4), the matrix 1,5-diaminonaphthalene (DAN) (Sigma Aldrich)

675   10mg/ml dissolved in 70% acetonitrile was applied onto the dried cells on the labtek slides by

676   using the same TM-Sprayer robotic sprayer. Spraying parameters were as following:

677   temperature=90 C°, number of passes=8, flow rate=0.07 ml/min, velocity=1350 mm/min, track

678   spacing=3 mm/min, pattern=CC, pressure=10 psi, gas flow rate=2 l/min, drying time=15 sec,

679   nozzle height=41 mm. The estimated matrix density was of 0.001383 mg/mm^2. For MALDI

680   imaging mass spectrometry, the glass slides with the dried cells on them were mounted onto a

681   custom slide adaptor and loaded into the AP-SMALDI source (Transmit, Giessen, Germany).

682   The MALDI laser focus was optimized manually using the source cameras with the focused

683   beam diameter estimated to be between 15.0 and 43.0 μm (mean equal to 29.9 μm, standard

684   deviation equal to 8 μm). The x-y step size (distance between the centers of ablation marks) was

685   set to 50 μM. For each pixel, the spectrum was accumulated from 30 laser shots at 60 Hz.

686   Negative mode MS analysis was performed in the full scan mode in the mass range of 200-1100

687   m/z (resolving power R=140000 at m/z 200) using an QExactive Plus mass spectrometer

688   (ThermoFisher Scientific). MS parameters in the Tune software (version 2.5 Build 2042,

689   ThermoFisher Scientific) were set to the spray voltage of 4.10 kV, S-Lens 80 eV, capillary

690   temperature 250 C. The data was converted from the RAW format into the imzML format

691   containing only centroided data using the ImageQuest software, v.1.1.0 (ThermoFisher

692   Scientific). Metabolite annotation was performed using the METASPACE cloud software

693   (http://metaspace2020.eu) implementing the bioinformatics methods for False Discovery Rate-

694   controlled annotation published by us earlier (Palmer et al., 2017) with the m/z tolerance of 3

695   ppm and FDR of 10%, 20%, and 50% against the HMDB metabolite database v2.5 (Wishart et

696   al., 2009).

697   **Post-MALDI microscopy to detect MALDI ablation marks**

698   The cells were imaged in bright-field microscopy after MALDI-imaging using the same

699   microscopy setup and parameters as described earlier in the pre-MALDI microscopy section to

700   define the positions of the ablation marks with respect to the fiducial marks.

701   **Association of laser ablation marks with single cells**

702   This is the key part of the method as it solves the challenge that single cells are not visible in the

703   post-MALDI microscopy images due to the opaque layer of MALDI matrix covering cells. Here,

704   ablation marks left by the MALDI laser were associated with single cells in three steps: a) cells

705   segmentation in the pre-MALDI microscopy images, b) detection of laser ablation marks in post-

706   MALDI microscopy images, c) matching between ablation marks and MALDI mass spectra and

707   d) co-registration of pre- and post-MALDI microscopy images to overlay the ablation marks

708   with the segmented single cells.

709   In step a), cells were segmented using a custom pipeline in the CellProfiler software (Carpenter

710   et al., 2006) where the DAPI staining channel was used to generate seeds for a region growing

711   algorithm detecting cells boundaries in the LD540-staining channel. In step b), we first denoised

712   the bright-field microscopy images by applying a low-pass filter in the 2D Fourier frequency

713   domain, in particular to exploit both the regular distances between ablation marks as well as the

714   repeated shape of the ablation mark itself. Then, we applied a contrast-enhancing filter (using the

715   *clip* function from the Python module *numpy*) and Otsu's thresholding method (Otsu, 1979) to

716   binarize the image (using the *imbinarize* function in Matlab). Then, we applied morphological

717   image analysis operations of closing and then opening to fill in the holes in the image and to

718   remove individual noisy pixels (using the *imclose* and *imopen* functions in Matlab). This

719   provided estimations of the centers of mass of each ablation mark (Figure S9). In step c), we fit a

720   theoretical rectangular grid to the ablation marks. The numbers of X- and Y- grid steps were

721   defined as set up during the MALDI acquisition. The center of the acquisition region was

722   considered as the center of the grid. The orientation of the grid with respect to the post-MALDI

723   microscopy image was optimized by finding an angle which resulted in the best overlap between

724   the grid lines and the detected ablation marks. The X- and Y-spacing of the grid were optimized

725   by minimizing the distance between the grid nodes and the center of mass of the nearest neighbor

726   ablation mark. Then, only ablation marks which were the nearest neighbors to the grid nodes

727   were taken and re-indexed (Figure S10). This provided X- and Y-coordinates for each ablation

728   mark associated with a collected MALDI spectrum. In order to improve estimations of the

729   ablations marks areas used later for normalization, their segmentation was further improved by

730   applying a custom region-growing algorithm implemented in Python. In step d), co-registration

731   of pre- and post-MALDI microscopy images was done based on the pen marks drawn on the

732   edge of the wells used as fiducials. We first segmented the pen marks in both pre- and post-

733   MALDI bright-field microscopy images using Otsu's intensity thresholding method. Then, we

734   used the basin-hopping optimization algorithm (Python implementation from the *scipy* package

735   v0.18.1) to find the best linear transformation matching the coordinates of the edges of the pen

736   marks between the pre- and post-MALDI images (Figure S10). The optimal linear

737   transformation was applied to the post-MALDI microscopy images to map the ablation marks to

738   the pre-MALDI microscopy images. The initial assessment of the co-registration quality and

739   overlaying of the metabolite intensities was performed in the `ili web app at http://ili.embl.de

740   (Protsyuk et al., 2018).

Single-cell intensity normalization

742   A normalized intensity of each metabolite in a single cell was constructed as follows. For each

743   cell, we considered all ablation marks overlapping with the cell area and selected the associated

744   ablation marks which overlap with the cell by over than 30% of their ablation area. The

745   metabolite intensities coming from an ablation mark were normalized by dividing them by the

746   ratio of the sampling area (defined as the number of pixels of the intersection of the ablation

747   mark and any cell region) to the area of the ablation mark. Finally, for each cell its normalized

748   metabolite intensities were calculated as the weighted average normalized intensities of the

749   associated ablation marks where the weights are defined as the ratio of the shared pixels (Figure

750   2). In order to account for the variations in permeabilization efficiency between the biological

751 replicates, single-cell LD540 fluorescence intensities were normalized by dividing them by the

752 median DAPI intensity (median over a well).

753 **Selecting intracellular metabolites**

754 We selected metabolite annotations corresponding to intracellular metabolites as follows. First,

755 for each ablation mark we assigned to it the inside-cells label having values either of zero or one

756 based on whether the mark has any overlap with any cell. Then, for each metabolite ion image,

757 its intensities were binarized to zero-one values by selecting a threshold leading to the highest

758 Pearson correlation with the inside-cells labels. The threshold value was found using the basin-

759 hopping optimization algorithm. In order to consider only intracellular metabolites for further

760 analysis, we selected those metabolite annotations whose binarized ion images were correlated

761 with the inside-cells labels with the Pearson correlation higher than 0.25. For the stimulated

762 dHepaRG experiment where three replicates for each of four conditions were obtained, we

763 considered the metabolite annotations which were shared by at least three samples (out of 12

764 overall) that led to 136 annotations. For each metabolite annotation, we pulled the ion images

765 with the m/z tolerance of 3ppm from the imzML files.

766 **Cell filtering and batch correction**

767 We filtered out 5% of cells with the lowest metabolite yield, namely the cells which had most

768 zero-valued metabolites annotations, following the approach well-accepted in single-cell

769 transcriptomics (Grün and van Oudenaarden, 2015) (Figure S11). In the stimulated HepaRG

770 experiment, this filtered out 1240 cells out of 23498 overall. In the stimulated HepaRG

771 experiment, to compensate for the batch effect between the biological replicates within each

772 condition, we applied the *combat* batch correction algorithm (Fortin et al., 2017) originally

773   developed for single-cell transcriptomics data using its open-source Python implementation

774   neuroCombat available at https://github.com/ncullen93/neuroCombat (Figure S4).

775   **Cell type classification for the co-culture experiment**

776   The assignment of the cell type based on the constitutive fluorescence of the cells (mCherry for

777   HeLa, GFP for NIH3T3) was done by finding a separating linear boundary between the two

778   populations (Figure 2A). The resulting cell types provided the ground truth labels for the Linear

779   Discriminant Analysis (LDA) performed using the Python *scikit-learn* LDA implementation

780   (version 0.19.1).

781   **LC-MS/MS validation of METASPACE annotations**

782   **Sample preparation:** Lipids and fatty acids were extracted using the Folch method (Folch et al.,

783   1957) with chloroform:methanol (2.5:1). For lipidomics analysis, the dried samples were

784   reconstituted in isopropanol:methanol (1:1) and injected 10uL into the LC-MS system. For

785   metabolomics analysis, metabolites were extracted in 80% methanol and directly injected 20uL

786   into the LC-MS system.

787   **LC-MS/MS methods for lipidomics:** All LC-MS/MS analyses were performed on a Vanquish

788   Ultra-High Performance Liquid Chromatography (UHPLC) system coupled to a Q-Exactive Plus

789   High Resolution Mass Spectrometry (HRMS) (ThermoFisher Scientific) with an electrospray

790   ionization (ESI) source operated in either positive or negative mode. The separation of lipids and

791   fatty acids was carried out using an Agilent Poroshell EC-C$_{18}$ column (3 x 50 mm; 2.7 μM)

792   maintained at 40 $^{\circ}$C at the flow rate of 0.26 ml/min. The mobile phase consisted of solvent A

793   (acetonitrile−water (4:6)) and solvent B (isopropyl alcohol−acetonitrile (9:1)), which were

794   buffered with either 10 mM ammonium acetate (for negative mode) or 10mM ammonium

795 formate acidified with 0.1% formic acid (for positive mode). The UHPLC gradient was set at

796 20%, 20%, 45%, 52%, 66%, 70%, 75%, 97%, 97%, 20%, 20% of solvent B at the time points 0,

797 1.5, 4, 5, 7, 8, 10, 12, 15, 16, 19 min, respectively. Fatty acids and lipids were detected with the

798 HRMS full scan at the mass resolving power R=35000 in the mass range of 100-1500 m/z. The

799 data-dependent tandem (MS/MS) mass scans for five most intense ions (TOP5) were obtained

800 along with full scans using higher energy collisional dissociation (HCD) with normalized

801 collision energies of 20, 30 and 40 units at the mass resolving power R=17500. The MS

802 parameters in the Tune software (ThermoFisher Scientific) were set as: spray voltage of 4 kV,

803 sheath gas 30 and auxiliary gas 5 units, S-Lens 65 eV, capillary temperature 320 ^{o}C and

804 vaporization temperature of auxiliary gas was 300 ^{o}C.

805 **LC-MS/MS methods for metabolomics**: LC-MS/MS metabolomics analysis was carried out

806 using an Xbridge BEH Amide column (100X 2.1 mm; 2.5 μM) maintained at 40 ^{o}C at the flow

807 rate of 0.3 ml/min. The mobile phase consisted of solvent A (7.5 mM ammonium acetate with

808 0.05% NH4OH) and solvent B (acetonitrile). The UHPLC gradient was set at 85%, 85%, 10%,

809 10%, 85%, 85% of solvent B at the time points 0, 2, 12, 14, 14.1, 6 min, respectively.

810 Metabolites were detected with HRMS full scan at the mass resolving power R=70000 in mass

811 range of 60-900 m/z. The data-dependent MS/MS mass scans were obtained along with full scans

812 using HCD of normalized collision energies of 10, 20 and 30 units which were at the mass

813 resolving power R=17500. The MS parameters in the Tune software (ThermoFisher Scientific)

814 were set as: spray voltage of 4 kV (for negative mode 3.5 kV), sheath gas 30 and auxiliary gas 5

815 units, S-Lens 65 eV, capillary temperature 320 ^{o}C and vaporization temperature of auxiliary gas

816 was 300 ^{o}C. Data was acquired in the full scan mode and MS/MS mass spectra for TOP5

817 precursor ions.

818 **LC-MS/MS validation of METASPACE annotations:** LC-MS/MS validation of lipid and

819 metabolite METASPACE annotations was performed either by comparing retention times, exact

820 m/z (MS) and fragmentation pattern (MS/MS) spectra with authentic standards or by matching

821 MS/MS spectra with the EMBL Metabolomics Core Facility (MCF) spectral library (available at

822 http://curatr.mcf.embl.de/) and public spectral libraries (LipidBlast, LIPID MAPS and mzCloud).

823 The details of annotation validation are summarized in Supplementary Data S1. The structural

824 annotation procedure for head groups (HD) and fatty acid side chains (SD) is described in details

825 in (Palmer et al., 2017).

826 **Data visualization**

827 All plots were generated in Python, version 3.6.2, by using the packages *matplotlib* 2.1 and

828 *seaborn* 0.8.1. The Python package *scikit-learn* 0.19.1 was used for the Principal Component

829 Analysis.

830 **Data availability**

831 All metabolite and lipid annotations and images are publicly available at the METASPACE

832 online knowledgebase (URL for the co-cultured and mono-cultured HeLa and NIH3T3 cells

833 from Figure 2, URL for the dHepaRG cells from Figure 3, URL for the dHepaRG cells from
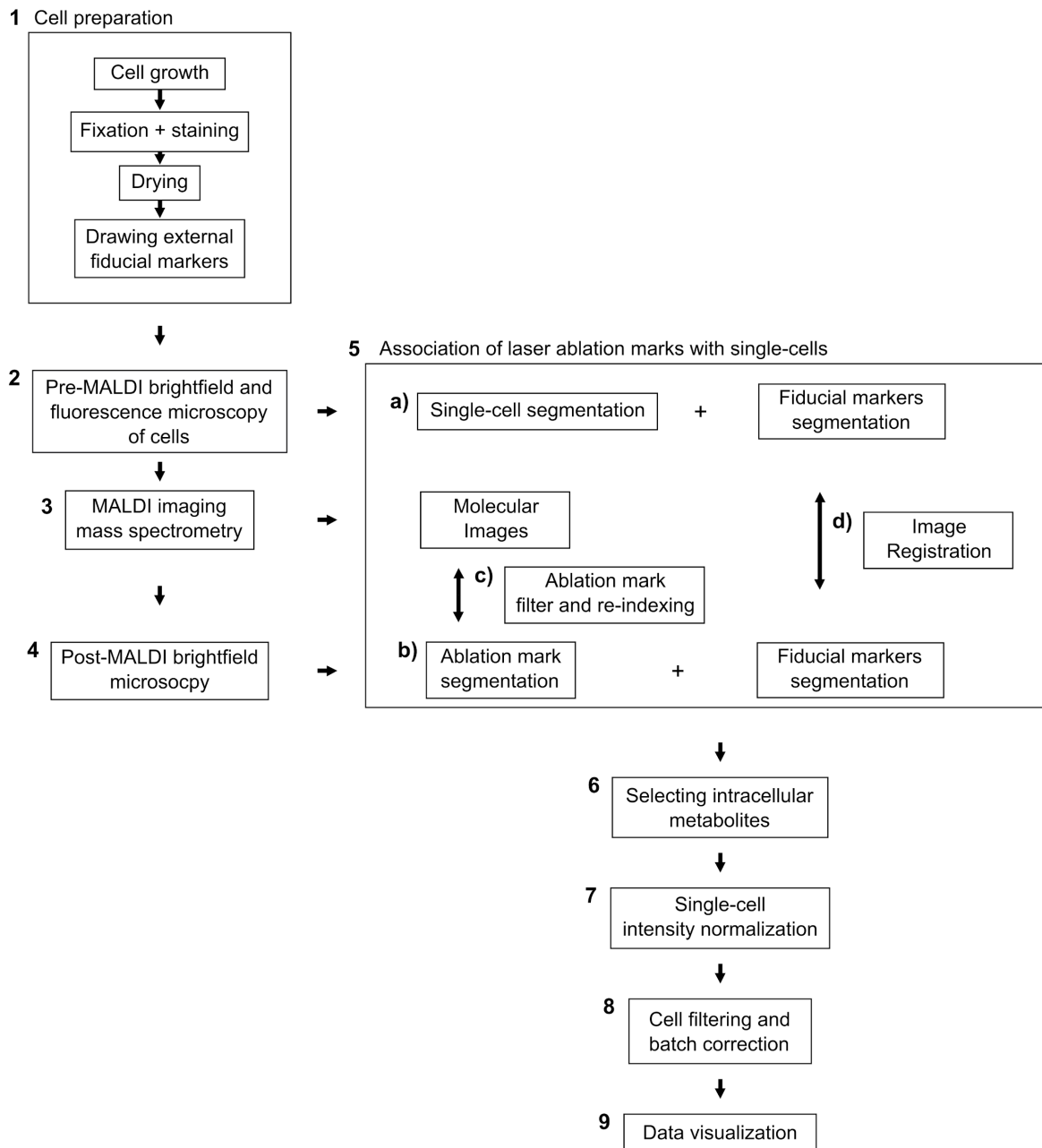
834 Figure 4).

835

836

837

838

839

840   # Supplementary Figures

1 Cell preparation

- Cell growth
- Fixation + staining
- Drying
- Drawing external fiducial markers

2 Pre-MALDI brightfield and fluorescence microscopy of cells

3 MALDI imaging mass spectrometry

4 Post-MALDI brightfield microsocpy

5 Association of laser ablation marks with single-cells

a) Single-cell segmentation + Fiducial markers segmentation

Molecular Images

c) Ablation mark filter and re-indexing

d) Image Registration

b) Ablation mark segmentation + Fiducial markers segmentation

6 Selecting intracellular metabolites

7 Single-cell intensity normalization

8 Cell filtering and batch correction

9 Data visualization

841

842   **Supplementary Figure S1.** Detailed workflow of the SpaceM method, see Figure 1 for a

843   visualization of the workflow supplemented with visual elements.

844

43
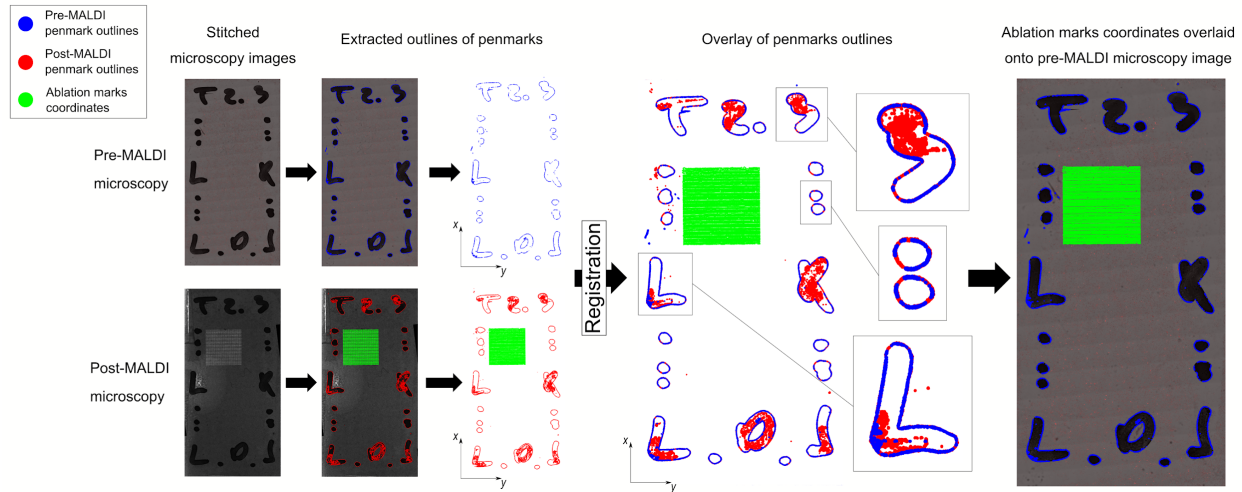
Supplementary Figure S2. Registration workflow of pre- and post-MALDI microscopy images. The area where MALDI-imaging was applied is shown in green. The features of the pen marks used as fiducials are shown in blue (for pre-MALDI microscopy images) or red (for post-MALDI microscopy images).
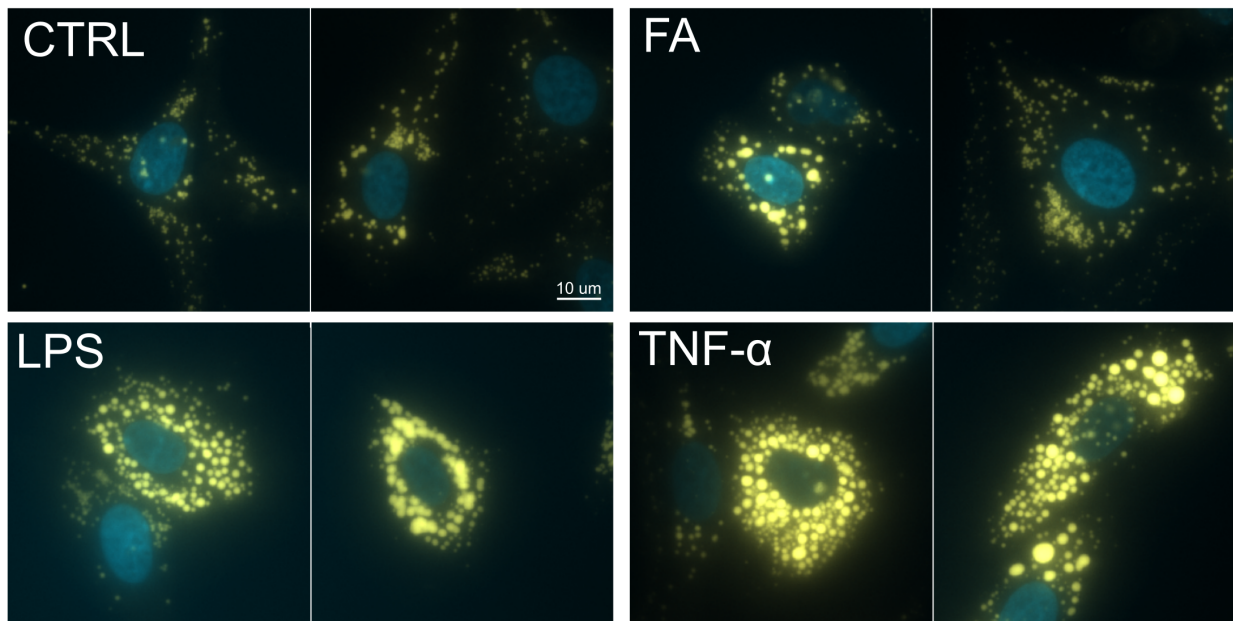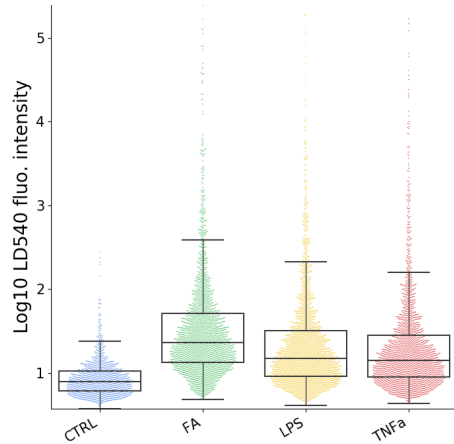

Supplementary Figure S3. Lipid accumulation, also known as macro-vesicular steatosis, in dHepaRG hepatocytes both inherently as well as under stimulation with: oleic and palmitic fatty

44

854   acids (FA), LPS in combination with the fatty acids, TNFα in combination with the fatty acids

855   (yellow for LD540, blue for DAPI) to highlight the localization around nucleus. Each subplot

856   shows two illustrative examples of cells.

857
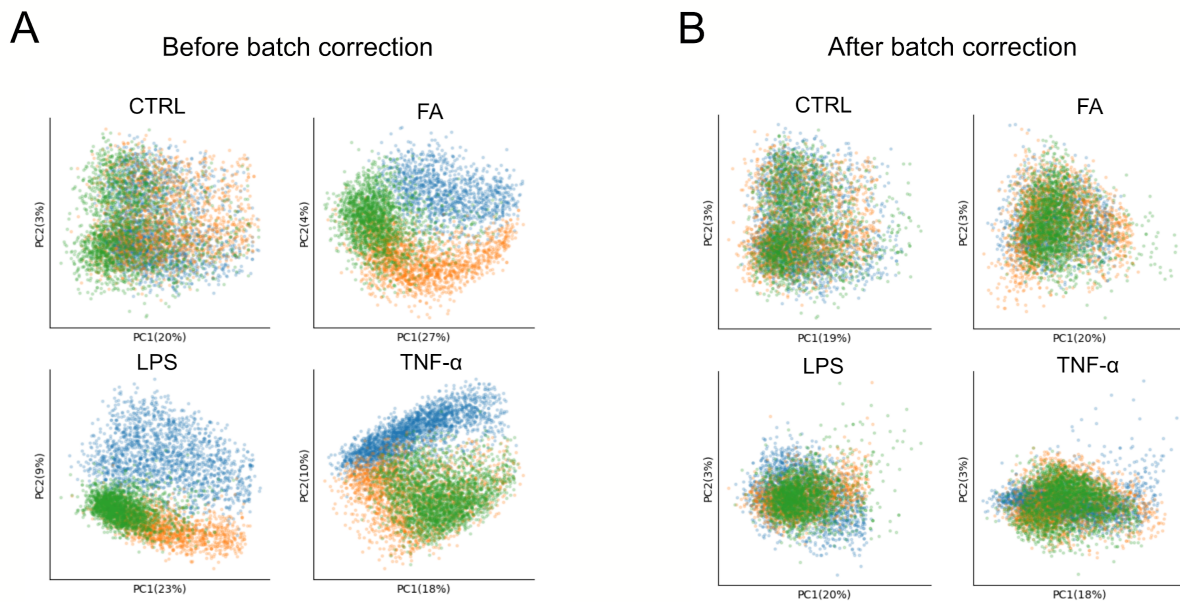
858

859   **Supplementary Figure S4.** Batch correction of variability between technical replicates in the

860   stimulated dHepaRG experiment by using the combat algorithm. The plots show a PCA plot of

861   the single-cell metabolic profiles with cells color-coded according to the replicate. **A:** Before

862   batch correction, **B:** after batch correction.

863

864

Supplementary Figure S5. Swarming plots of single-cell LD540-fluorescent intensities of stimulated dHepaRG cells for each condition indicating increased lipid accumulation upon stimulation with FAs, LPS, and TNFα.

868

869
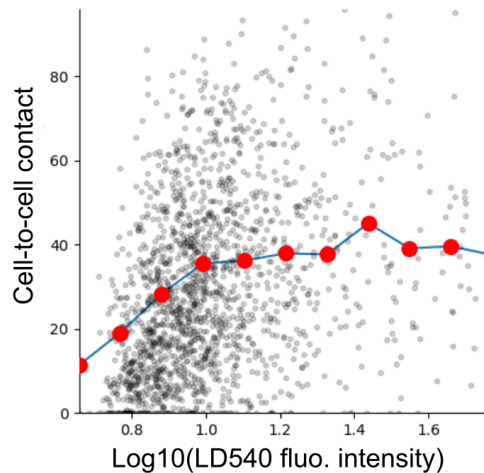
Supplementary Figure S6. Scatter plot of the LD540 fluorescent intensity and cell-cell contact for one replicate of dHepaRG cells stimulated with TNFα in combination with oleic and linoleic acid (n=1830), with the Spearman r_s 0.34, p-value 9.18e-4. The LD540 intensities were thresholded at the 95% percentile. Red dots visualize average values for regularly-spaced bins of LD540 fluorescence intensity.
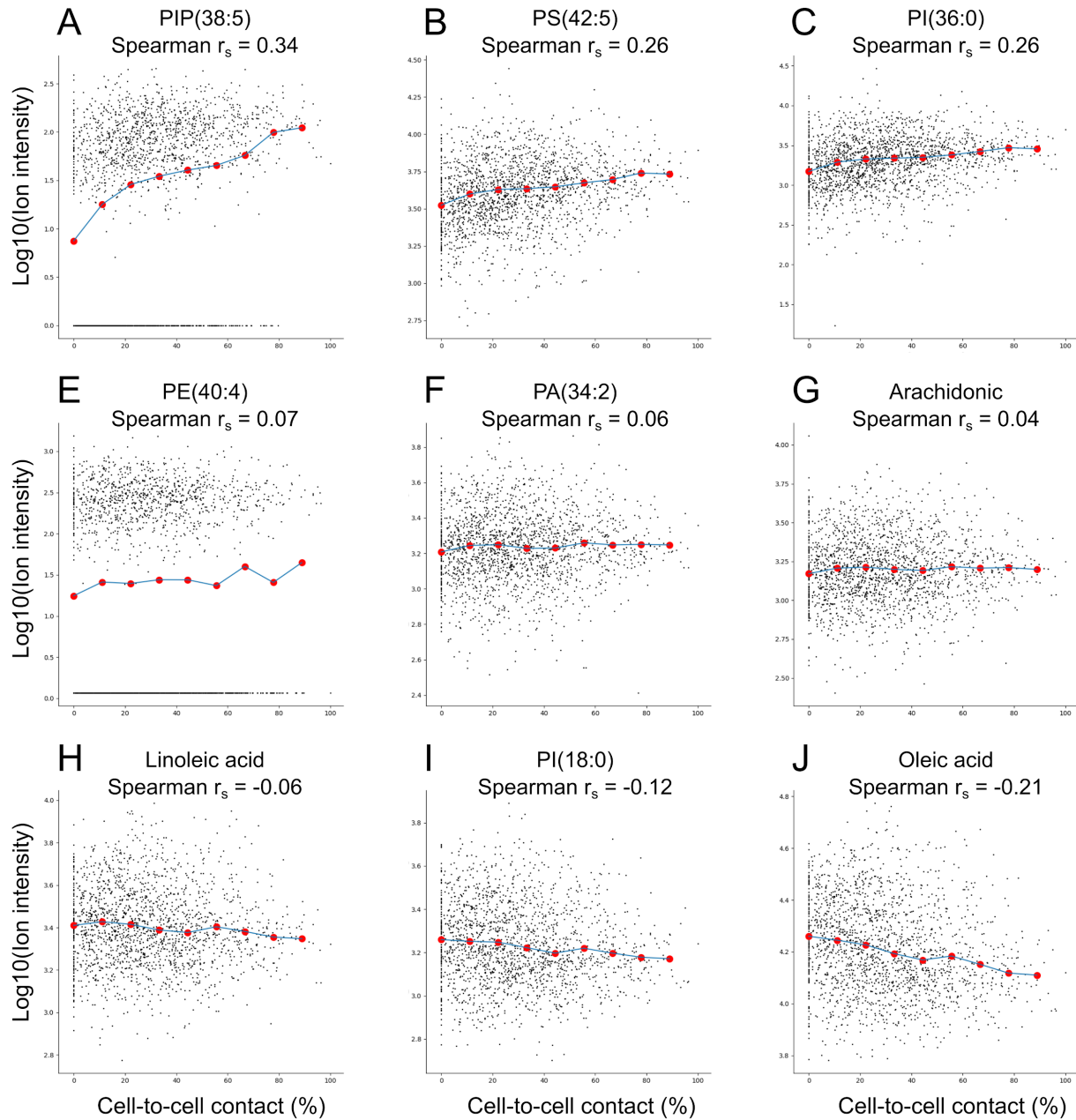
46
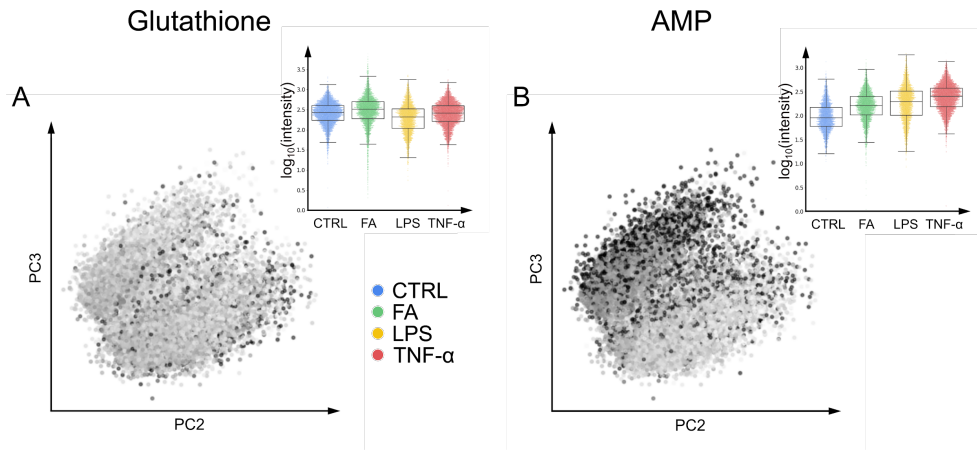
Supplementary Figure S7. Observed relationship between local crowding and intracellular metabolite intensity. One dot represents one cell. Red dots represent average intensities for regular bins of local crowdedness. The data are coming from one replicate of the TNFα condition (1830 cells).
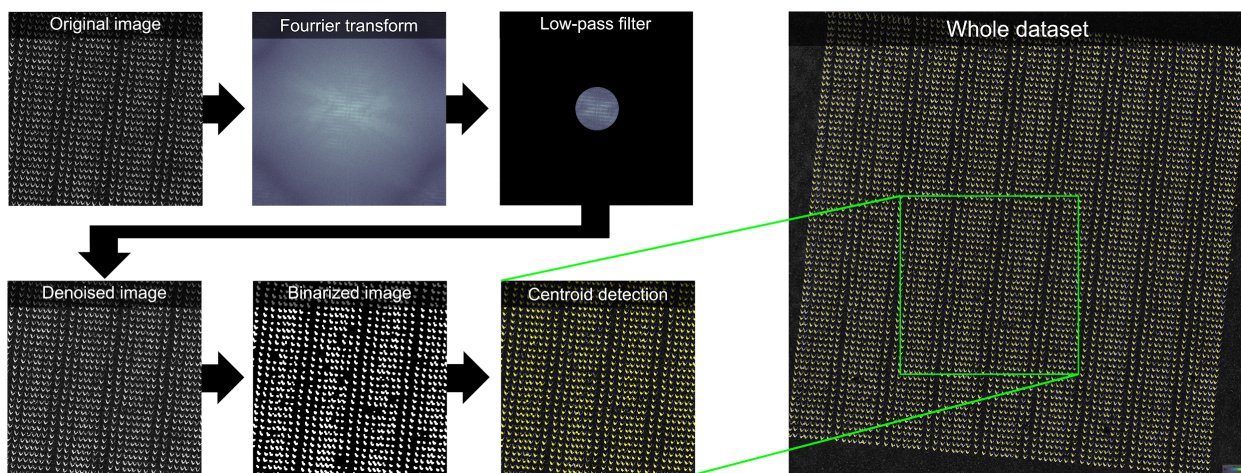
Supplementary Figure S8. Mapping of intensities of the small molecules glutathione and AMP onto the principal components of z-scores of the single-cell metabolic profiles of dHepaRG cells from the CTRL, FA, LPS, and TNFα conditions (similar to Figure 3B-D).
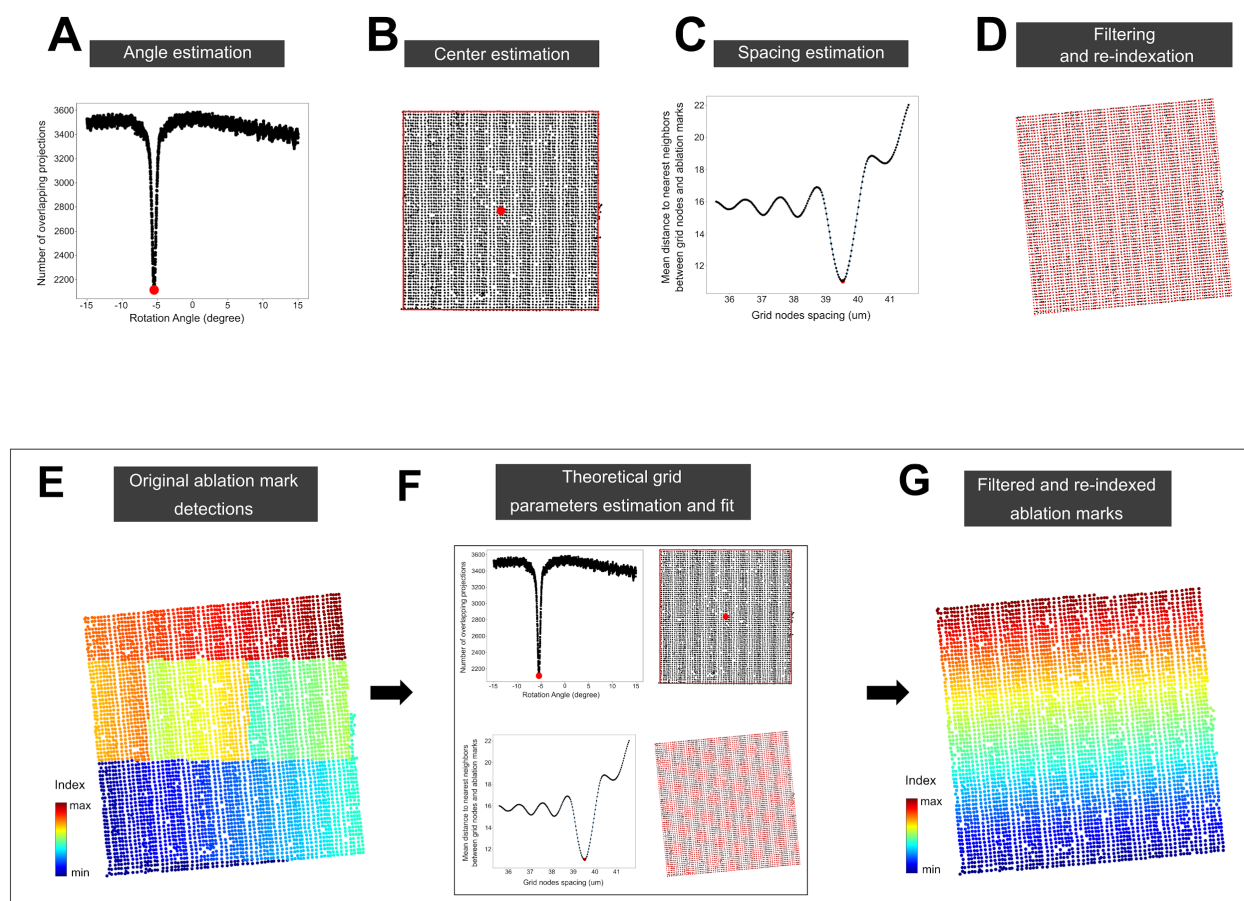

Supplementary Figure S9. Illustration of the procedure for detection of laser ablation marks in post-MALDI microscopy images.

Supplementary Figure S10. Illustration of the procedure for fitting a theoretical rectangular grid to the ablation marks segmented in the post-MALDI microscopy images. The three parameters of the grid are estimated using the ablation marks coordinates. In A, the angle is estimated by counting the number of non overlapping ablation marks coordinates projections of the X axis for different rotation angle. The minimum number of projection is reached for an alignment angle with the projection axis. In B, the center of the grid is estimated from the extrema of the ablation mark coordinates. The spacing of the grid nodes is estimated in C by measuring the mean distance to the nearest ablation mark to each grid node. The chosen grid node spacing is leads to smallest mean distance to the ablation mark coordinates. The re-indexing in D is done by choosing the closest ablation mark coordinates from the grid nodes constructed using the parameters defined before (the grid nodes are shown in red, their nearest

49

903   ablation mark coordinates are shown in black). In E, the ablation mark coordinates are color

904   coded by their index. An illustration of the different steps for fitting a grid onto the ablation mark

905   coordinates as well as the re-indexing is shown in F. In G, the re-indexed ablation mark are

906   shown. and re-indexing them to associate each detected ablation mark with a MALDI spectrum.

907
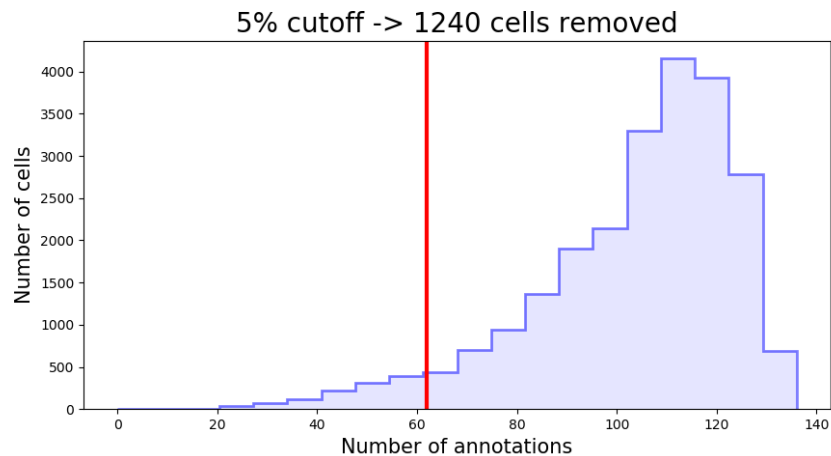
908

909   **Supplementary Figure S11.** Filtering out poor quality cells for the dHepaRG experiment

910   (Figure 4). The cells with low number of METASPACE annotations (less than the 5% lower

911   percentile of the distribution) were removed.

912

913

914

915

916 # Supplementary Table

Sample ("Condition"_ "Replicate number")	Matrix application			MALDI-imaging		
	Date; Time	Room temperature (°C)	Room humidity (%)	Date; Time	Room temperature (°C)	Room humidity (%)
FA_1	22.06.17; 1.40pm	23.1	58	22.06.17; 2.01pm	23.1	50
LPS_1	22.06.17; 4.10pm	23.2	60	22.06.17; 4.30pm	23.7	49
FA_2	24.06.17; 12.40am	21.9	52	24.06.17; 1.00pm	23.3	47
LPS_2	24.06.17; 3.50pm	21.9	53	24.06.17; 4.10pm	23.5	47
Untreated_1	25.06.17; 6.30am	21.9	52	25.06.17; 7.00am	23	48
TNFa_1	25.06.17; 12.15am	22.1	60	25.06.17; 3.30pm	23.6	51
FA_3	25.06.17; 6.30am	21.9	58	25.06.17; 10.00am	23.1	47
TNFa_2	25.06.17; 9.15am	21.9	60	25.06.17; 9.35am	23.1	52
Untreated_2	25.06.17; 12.41pm	21.5	55	25.06.17; 4.00pm	23.1	47
Untreated_3	25.06.17; 12.41pm	21.5	55	25.06.17; 1.00pm	23.1	46
LPS_3	28.06.17; 2.59pm	21.1	63	28.06.17; 6.30pm	23.3	48
TNFa_3	30.06.17; 2.30pm	21.1	50	30.06.17; 6.41pm	22.6	44

917 **Supplementary Table S1.** *Experimental design and ambient conditions for matrix application*

918 *and MALDI-imaging analysis of dHepaRG samples.*

919

920   ## Supplementary Data (attached as a separate file)

921   ***S**upplementary Data S1. LC-MS/MS validation of METASPACE metabolite annotations.*

922   *Summary and detailed information about LC-MS/MS validation of METASPACE annotations*

923   *including MS/MS and chromatographic information.*

924